Coupling Plasmonic Cavities to Quantum Emitters

Permanent link

Terms of Use

Share Your Story

Accessibility

Coupling Plasmonic Cavities to Quantum Emitters

A DISSERTATION PRESENTED
BY
I-CHUN HUANG
TO
THE DEPARTMENT OF THE SCHOOL OF ENGINEERING AND APPLIED SCIENCES

IN PARTIAL FULFILLMENT OF THE REQUIREMENTS
FOR THE DEGREE OF
DOCTOR OF PHILOSOPHY
IN THE SUBJECT OF
APPLIED PHYSICS

HARVARD UNIVERSITY
CAMBRIDGE, MASSACHUSETTS
MAY 2017

Thesis advisor: Professor Marko Lončar   I-Chun Huang

Coupling Plasmonic Cavities to Quantum Emitters

Abstract

Nano-plasmonic devices can have a wide variety of applications that rely on strongly enhanced optical fields confined well below the diffraction limit. The applications could be surface-enhanced Raman scattering, nanoscale nonlinear optics, optical tweezing, large Purcell enhancement and fluorescence enhancement. Here first we demonstrated the fabrication of 10-nm gap silver bowtie apertures based on e-beam lithography and lift-off process, which are conventionally fabricated by lower-throughput focused ion beam. The aperture can have mode area as small as $0.002\,(\lambda/n)^2$, showing that they are good plasmonic nano-cavities for emitter coupling. Then, due to highly concentrated field, these bowtie apertures were used to optically trap individual, 30 nm silica coated quantum dots (scQD), with a relatively low continuous wave trapping flux of 1.56 MW/cm^2 at 1064 nm. This platform might enable single quantum dot absorption spectrum measurements.

Last, we applied plasmonic nano-cavities for other quantum emitter, silicon vacancy (SiV) center in diamond. We designed circular plasmonic apertures to have Purcell enhancement on SiV center in diamond. SiV centers inside can have lifetime as short as 0.2 ns, which represents a $\sim$9-fold reduction over a $\sim$1.8 ns value typical for SiV in bulk diamond. Due to low internal quantum efficiency of SiV center, the Purcell enhancement could be larger than the measured lifetime reduction. Also, SiV in the plasmonic apertures can have linewidth as narrow as 330 MHz, which is comparable to the

transform-limited linewidth. The spectral diffusion is within the linewidth ($\pm$ 100 MHz), showing

that our devices can have applications in quantum optics.

Contents

Author List

1. The following authors contributed to Chapter 1: Jeffrey Holzgrafe, Russell A Jensen, Jennifer T Choy and, Moungi G Bawendi.

2. The following authors contributed to Chapter 2: Russell A Jensen, Ou Chen, Jennifer T Choy, Thomas S Bischof, and Moungi G Bawendi.

3. The following authors contributed to Chapter 3: Srujan Meesala, Cleaven Chia, and Jeffrey Holzgrafe.

Listing of figures

ix

For Li-Yun Hsieh and Sheng-Nan Huang, my loving and supportive parents

For Chung-Tai Huang and I-Pin Huang, my brothers and childhood companion

Acknowledgments

First of all, I want to thank my PhD advisor, Prof. Marko Lončar. I really enjoyed working in his lab a lot. Marko's advising style is very encouraging, which is absolutely important because there are always many frustrations in PhD life. Also, Marko gives all of us a lot of freedom to do our preferred research independently. This trained me to become an independent researcher, which is important for my future career.

I would also like to thank my committee members: Profs. Federico Capasso and Evelyn Hu. I always admire Federico as a great scientist - a person who can explain physics in an intuitive way. I enjoyed taking Federico's class. His questions are always inspiring and great. Evelyn is also my role model. She dedicates herself to research and gave me great comments on my dissertation. I also appreciated that they have helped create a great photonics family at Harvard, and it is always a pleasure to discuss research with people in their groups.

I would like to thank my group members. Lončar guys are all awesome, talented and willing to help and teach me. I would like to thank my mentor in my early PhD life: Jen. Jen is known for being the nicest person in Loncar group. I am fortunate to have had her as my early mentor. She guided me into the field of plasmonics and gave me her ongoing project. She helped improving my resumes even years after she graduated. Then I would

like to thank Cheng. We hung out, discussed research and life a lot. I learned a lot from talking to him, whether academic or not. He is also a role model for me, a person who can execute any plan effectively. I would also like to thank Young-Ik. Young-Ik is one of the funniest people to hang out with. He has lots of special and great thoughts, both on research and life. He is a strong person and cares a lot about other people as well. Young-Ik is also a great mentor and giver. I always learned a lot whenever I asked him for fabrication advice. Then I want to thank Anna for being a great labmate. Anna is willing to help all the time, correct my slides or writing, including these acknowledgments! She is also the person who listened to me about my frustrations, and I am happy to have her in the lab. I would also like to thank Haig, a very interesting and confident person, always offering and willing to help. Mian is a very knowledgeable and smart person. Whenever I talked to him, he always could come up with a completely new perspective or thought, which is very inspiring. Srujan is a great physicist. He helped a lot in solving problems that came up in the SiV project, and in defining the direction of my project. I would also like to thank Cleaven, who helped me implement the simulation part of plasmonic cavity used for SiV center coupling. I would like to thank Shota as well. He is really nice and it is especially great to discuss fabrication with him. Jeff helped me a lot in some plasmonic cavity simulations and setup. I would like to thank him as the best intern I have ever had. Mike is the leader in our diamond projects. He also keeps the lab organized. I did not work with Vivek directly, but he is definitely the per-

tion.

Then I would also like to thank my friends in SEAS. SEAS is a great community to make awesome friends. Thanks to Nan for holding those memorable BBQ events. He introduced us lots of new experiences: fishing, Broadway shows, and good restaurants. More importantly, we shared all those funny moments. Then I want to thank Yang Li. We hung out together a lot and shared lots of academia and life experiences. I would also like to thank Jonathan. He is such a knowledgeable person and gave me pretty good research advises. I would also like to thank Jingyee, Huiliang, Alex Zhang and Alp for their support.

I would also like to thank my Taiwanese friends here in Boston. Pei-Fen is a great friend all the time. We can understand each other easily, and I enjoyed our countless conversations. I would also lilke to thank How-Huan, Feng-En, and Chung-Yu for accompanying me through these 6 years. I would also like to thank to Aaron and Yu-Chieh. Aaron shared lots of his job hunting experiences and even lent me his suit for the defense and interviews.

I would also like to thank my dorm friends. Prahar is always so positive and energetic. It is always a great pleasure to hang out with him. I would also like to thank Albert, LT, Stacy, Hiro and Ceyhun. I enjoyed hanging out, having meals and celebrating when we all lived in the dorm. The memories are all precious to me. I also want to thank Arlene for the guidance towards getting my PhD degree.

I also want to thank my friends back in Taiwan. Thanks to Yu-Ting Chen and Chia-Jung

Hu, two of my best old friends. As people who also struggle in the foreign countries, Yu-Ting and Chia-Jung shared lots of common feelings and experiences. Thanks for supporting me all along through this. I would also like to thank to Po-Tsung. Po-Tsung is like my mental counselor even when I was in Taiwan. He helped me out when lots of problems were thrown onto my life. I would also like to thank to Tai-You and Yung-Chen for being my teammates in gaming.

Finally I would like to mention the most important people in my life: my family. I would like to thank my dad, Sheng-Nan Huang. I would also like to thank my two brothers: Chung-Tai Huang and I-Pin Huang. Especially my big brother Chung-Tai gave me a lot of support. I would like to thank my mom, Li-Yun Hsieh. She is always strong tackling the things in life. She gave me countless support towards my decision of studying PhD abroad. This degree could not be pursued and completed without her. Thank you, my mom.

1

Introduction

Metal nanostructures separated by nanometer-scale gaps can have plasmonic resonances which locally enhance the optical field intensity by several orders of magnitude in sub-diffraction volumes[9,10]. These nano-plasmonic devices have a wide variety of applications in systems that rely on strong optical fields, such as surface-enhanced Raman scattering[11,12], nanoscale nonlinear optics[13,14,15], optical tweezing[16,17], fluorescence enhancement[18], and large

Purcell enhancement of quantum emitters[19,20]. Plasmonic field enhancement becomes much stronger as the gap size is reduced to nanometer scale. This effect has been demonstrated in various applications: Purcell enhancements larger than 1000 were achieved using silver nanowires or nanocubes on metal films with spacing of 5 to 15 nm[19,20]; surface-enhanced Raman scattering increases by orders of magnitude when the gap of gold dimers decreases[12] because of the fourth power dependence of electric field; and optical trapping simulations show that tapered 5-nm gap coaxial apertures could trap 2-nm dielectric particles with reasonable laser powers[21]. Thus, a controllable, high yield method to fabricate plasmonic structures with small critical dimensions is a key enabling technology for the applications.

In this thesis, we demonstrated the fabrication of narrow-gap plasmonic apertures, and applied them in optical tweezing and Purcell enhancement of solid state quantum emitters. In chapter 2, rather than using the conventional focused ion beam, we fabricated 10-nm gap plasmonic bowtie apertures using e-beam lithography and lift-off. This large-scale fabrication enables us to have cavity design optimization and experimentation. In chapter 3, we applied our bowtie apertures to optically trap 30 nm quantum dots with moderate trapping laser intensity of 1.56 MW/cm² at 1064 nm. This platform could be used to study single dot broadband absorption spectrum. In chapter 4, we fabricated plasmonic nanocavity to have Purcell enhancement on silicon vacancy center in diamond. Maximum lifetime

reduction of 9 was measured. We also observed the SiV with transform-limited linewidth and highly reduced spectral diffusion. This shows that our devices could enhance SiV fluorescence while preserving quantum properties, which is critical towards future quantum applications.

2

Narrow-Gap Plasmonic Apertures

Figure of merits like field enhancement or mode volume in plasmonic structure usually critically depend on the metal gap distance. There has been much work done to achieve ultrasmall gaps in metal structures. Currently, sub-10-nm gap plasmonic nanostructures can be fabricated by atomic layer deposition followed by ion milling[22], angled deposition[23], self-assembly of nanoparticles[24], chromium expansion with a second lithography[25], and

template stripping from a silicon substrate[26,27]. Among all plasmonic nanostructures, the bowtie apertures (see Figure 2.1) are one of the more widely used plasmonic resonator structures, having been applied to optical trapping[28,29], sub-diffraction optical lithography[30], and molecular fluorescence enhancement[31]. Focused ion beam (FIB) milling is a technique often used to achieve narrow-gap plasmonic aperture devices. For example, Ga^+- FIB has been used to fabricate coaxial[32] and bowtie[33] apertures with gap sizes down to 30 nm. However, realizing smaller gaps can be challenging due to the finite ion beam size and ion-substrate interaction[32]. Recently researchers have used milling-based He^+-ion lithography (HIL) to produce apertures with even smaller gap sizes, down to 8 nm in coaxial shapes[32] and 5 nm in dimers[34,35,36]. HIL provides better spatial resolution and lateral smoothness than Ga^+ based FIB[32]. However, both of these techniques are serial in nature, and fabrication of large arrays of devices is challenging. Electron beam lithography (EBL), followed by lift-off or ion milling, is a more scalable approach, capable of producing high resolution features at much a higher production rate. For example, sub-10nm features were recently developed on hydrogen silsesquioxane (HSQ) EBL resist[37,38,39]. Furthermore, metal structures with sub-10 nm features have been demonstrated on silicon[40] and silicon nitride membrane substrates[41,42]. However, the thickness of the metal layer that could be patterned (by lift-off) in these works was limited to $\sim$ 30 nm[40], which is not sufficient to support non-zeroth order Fabry-Perot type resonances in bowtie nanoapertures[43,44]. Furthermore,

thicker metal films are needed to tune the resonance of these modes.

In this work, we developed a modified EBL lift-off process to fabricate large arrays of bowtie apertures with nanoscale gaps and resonances that can theoretically be tuned by controlling the thickness of the metal layer[45]. Using this approach, we fabricated 150 nm thick silver bowtie apertures with gap sizes down to 11 nm (aspect ratio $\sim$ 14 : 1). This is better than what has previously been achieved with coaxial metal aperture using Ga^{+}-ion based FIB (30 nm gap, aspect ratio $\sim$ 3 : 1) and is comparable to results obtained with He based FIB (8 nm gap, aspect ratio $\sim$ 13 : 1)[32]. Besides, the mode area of the 11-nm-gap aperture is estimated to be as small as 0.002 $(\lambda/n)^2$ using numerical modeling. More importantly, our approach is scalable and allows for realization of many devices in parallel. For example, we show that by varying the geometry of the bowties, resonances can be designed to span wide wavelength range, from 470 to 687 nm on one sample. Quality factors of $\sim$ 12 were measured. We believe that the devices demonstrated in this work will find application in studying and engineering light-matter interactions.

2.1   DESIGN

Figure 2.1 (a) shows the schematic of the designed bowtie aperture in thin silver film, assuming the sidewall is vertical. The light incident on the aperture having polarization across the gap will be mainly coupled to the fundamental gap mode, which is concentrated inside
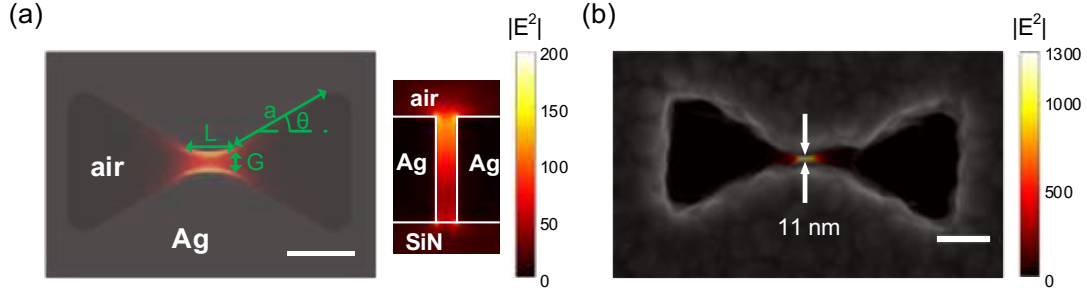
Figure 2.1: (a) The schematic and numerical modeling of the designed bowtie and the fundamental gap mode field intensity distribution. Side view field profile shows the Fabry-Perot like resonance with one node inside. G is the gap width, L is the gap length, a is the arm length, and ϑ is the angle of the arm. Here L = 82 nm, G = 30 nm, a = 150 nm, and ϑ = 30°. (b) SEM image of a bowtie aperture with G = 11 nm, overlapped with field intensity enhancement profiles at its resonance wavelength. It can be seen that this aperture can have an intensity enhancement as high as 1300. The scale bars are all 100 nm.

the gap. Figure 2.1 (b) shows the mode profile for the 11 nm-gap aperture at its resonance wavelength, obtained using three-dimensional (3-D) finite-difference time-domain (FDTD) simulations (Lumerical), overlaid on the scanning electron microscope (SEM) image of the fabricated structure. The maximum field intensity inside the aperture is found to be $\sim 1,300$ times stronger than the incident light outside the aperture, according to the simulations. Using the definition of energy density in dispersive medium and mode area[46], notice that because silver is a highly dispersive medium in visible region, the electric field energy density formula is modified to have derivative on ε as well:

$$A_{\text{mode}}(x_\circ, y_\circ) = \iint \Re\left[\frac{\partial \omega \varepsilon(x,y)}{\partial \omega}|E(x,y)|^2\right] dxdy \left/ \Re\left[\frac{\partial \omega \varepsilon(x_\circ, y_\circ)}{\partial \omega}|E(x_\circ, y_\circ)|^2\right]\right. \quad (2.1)$$

The mode area can be calculated to be as small as 0.002 $(\lambda/n)^2$ (normalized to the field at the center of the aperture, (x_0, y_0)). λ is the aperture resonance wavelength, which is 840 nm. This means the mode area is only 38×38 nm^2. We note that the gap mode of bow-tie apertures is always guided no matter how small the gap is (as long as the guided wavelength is below the cutoff, which is defined by the aperture outline), which is not the case in circular apertures[47]. This means that the mode area can be made extremely small and is only limited by the extent to which small gaps to be fabricated. However, a trade-off between mode area and loss due to absorption by the metal needs to be considered.

If we solve the Maxwell equation on the interface between a dielectric and metal, we can find a special TM mode. This special TM mode is a surface plasmon polariton (SPP) mode. One important feature of the SPP mode is that it is exponentially decayed in both dielectric and metal material, so that it is extremely confined on the interface. This results in the capability of high field enhancement and small mode area, which gives plasmonics having applications in the areas mentioned above. Its dispersion curve is show in Figure 2.2[1]. We can see its wavevector is larger than the free space one, so the mode index is larger than the dielectric one.

Now we see a common structure which is metal-insulator-metal (MIM). The SPP modes on both interfaces couple with each other and form new even and odd modes. From an energy confinement point of view, the fundamental odd mode is more interesting because it
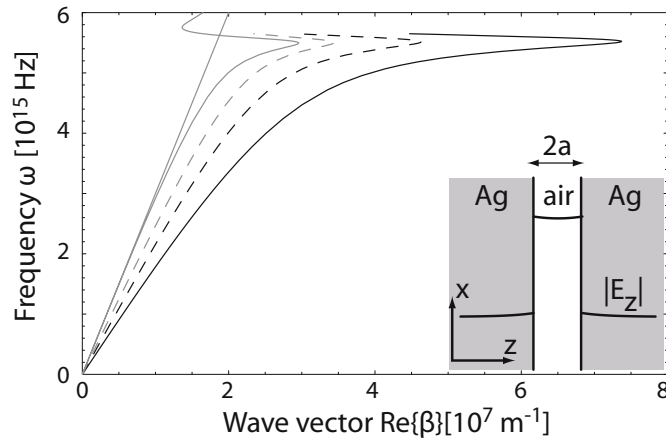
Figure 2.2: Calculated dispersion curve of the fundamental coupled SPP mode of a silver-air-silver structure for an air core size of 100 nm (dashed gray curve), 50 nm (dashed black curve), and 25 nm (solid black curver). The dispersion of SPP mode in single silver-air interface is also shown (solid gray curve) [1].

has no geometric cutoff when the dielectric core size approaches to zero. The odd mode is the one with higher index than the SPP mode. When the dielectric core size decreases, the coupling becomes stronger and the index becomes higher (Figure 2.2). We also saw this in our apertures, which will be discussed in the section 2.4. The gap mode in our bowtie apertures is similar to this odd mode in MIM structure: It is also an odd mode and the energy is concentrated and uniformly distributed inside the gap. This feature gives our bowtie plasmonic apertures great opportunities to couple with quantum emitters.

The wave-guided gap mode is sandwiched between two interfaces - one between the air and aperture and the other between silicon nitride and aperture. We used a fabricated air bowtie aperture in a 250-nm thick Ag film as an example. The transmission spectrum of

9

the fabricated bowtie is simulated and has two Fabry-Perot resonances at 3357 and 1151 nm

(Figure 2.3). From the number of nodes in their cross section mode profile, we can judge

that they are Fabry-Perot resonances with 0th and 1st order. The 0th order resonance is also

called the antenna resonance, which totally depends on the aperture/antenna size[43]. If we

want to shift the 0th order resonance to visible region, the aperture size would be too small,

and it is tricky to fabricate. Because we planned to couple these plasmonic nano-resonators

to visible quantum emitters, we chose to utilize the 1st order resonance.

2.2   FABRICATION

The fabrication procedure used is outlined in Figure 2.4 (a). Our devices are fabricated

on 50 nm thick silicon nitride membranes in order to reduce the resist exposure to back-

scattered electrons, and thus improve the resolution of our EBL step. We spin-coated the

negative-tone HSQ electron resist (FOX-16, Dow Corning), forming a 0.8 to 1 μm thick

resist film on top of 50 nm silicon nitride membrane with a silicon scaffold (Norcada InC.).

EBL is used (Elionix ELS-F125) to pattern bowtie apertures, and the e-beam dosage is from

3360 to 4128 μC/cm². Then, the sample was developed in tetramethylammonium hydrox-

ide for 17 seconds, leaving behind $\sim$ 800 nm tall bowtie posts. The e-beam resist post side-

wall is almost vertical, which implies that there is virtually no electron back-scattering from

the substrate (left of Figure 2.4 (b)). Next, electron beam evaporation (Denton) was used to

(a)

28 nm

(b)

Air Transmission

1st order

0th order

T (A.U.)

Wavelength (nm)
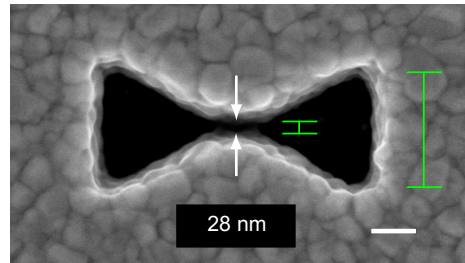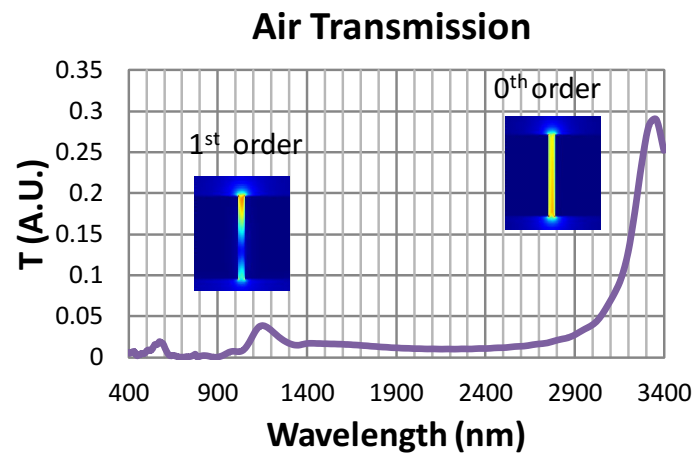
Figure 2.3: (a)The SEM picture of the bowtie, fabricated on 250nm Ag film. (b)The transmission simulation of the bowtie aperture in (a). The aperture acts as a low Q and small mode volume cavity. It shows mainly two resonances in 1151nm and 3357nm. The insets are their cross section mode profile, proving that they are Fabry-Perot like resonances. The 1st order one can be tuned by film thickness. The 0th order resonance can be tuned by the aperture overall size.

evaporate a 2 nm layer of titanium followed by a 150 nm layer of silver. Figure 2.4 (b) shows that silver nanoparticles are deposited on the resist sidewall as well, which causes the incomplete lift-off process. To mitigate this, we used a swab soaked with IPA to gently scrub the sample after the evaporation. This step breaks and removes the silver particle-coated posts just above the silver surface. Finally, we submerged the sample in 5:1 BOE (buffered oxide etch) for 130 seconds to remove the resist inside the aperture. Using this procedure we could increase the yield of clear bowtie aperture production to almost 100% while realizing thousands of devices on a single chip. We also demonstrated that this method is suitable for realization of bowtie apertures in thicker silver films: for example, we could fabricate 28 nm-gap bowtie apertures in 250 nm thick silver film (Figure 2.5) and 8 nm-gap apertures in 90 nm thick silver layer(Figure 2.6). This is very challenging to accomplish using focused ion beam milling.

A few heuristics about e-beam writing bowtie posts are also worth mentioning. If the e-beam dosage is too large, the gap size G and aperture itself will increase. However if the dosage is too low, the gap will be closed and the two wings of the bowtie will be disconnected. For the same dosage, G reduces as gap length L increases (due to the proximity effect), and can eventually become zero (the wings get disconnected) if L is too large. Therefore, using the same EBL pattern, the gap size can be tuned by controlling the dosage and gap length. In general, 20-nm gap bowties are easily achievable while the yield of 10-nm gap

(a)

HSQ
Silicon Nitride
Silicon

1. E-beam write posts   2. Evaporate Ag

57 nm

Ag
Silicon Nitride
Silicon

3. Scrubbing   4. BOE 5:1 etch

35 nm

(b)
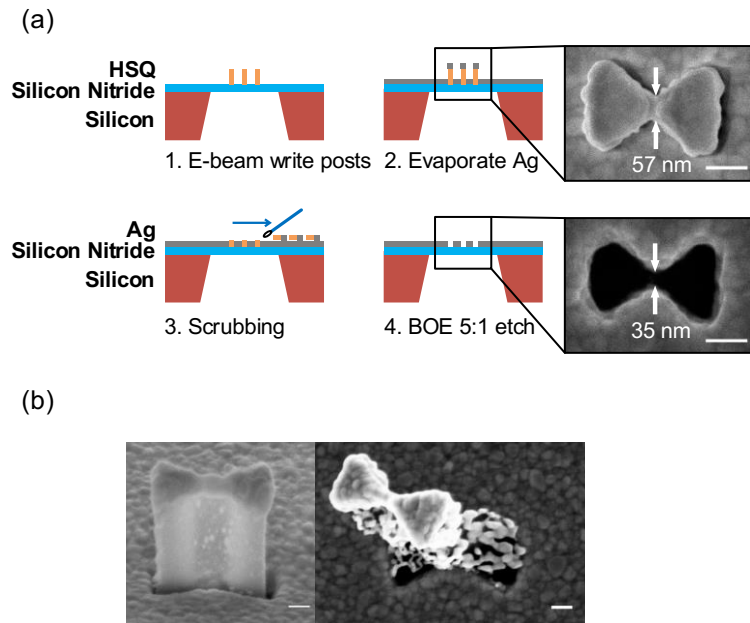
Figure 2.4: (a) Schematic of the modified lift-off process used to fabricate our devices. The two SEM images are the top view of the device in step 2 and 4. Notice that the final gap is smaller than the gap of the metal deposited on top of resist. (b) Left: Side view of the device in step 2. The metal evaporation step results in silver particles being deposited on the sidewall, which can compromise the lift-off process. Right panel shows the particles aggregating around the aperture after the lift-off, thus rendering the aperture unusable. To prevent this scrubbing with IPA soaked swab is used, as shown in (a). The scale bars are all 100 nm.
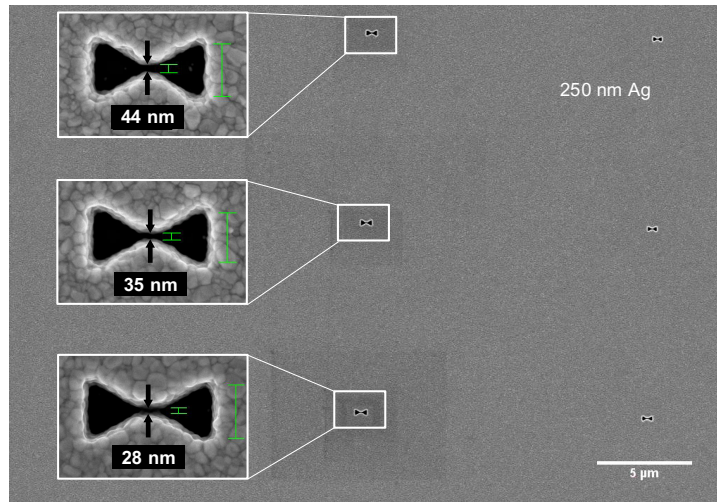
Figure 2.5: The bowtie apertures fabricated in 250 nm thick silver film. The smallest gap we can achieve is 28 nm.
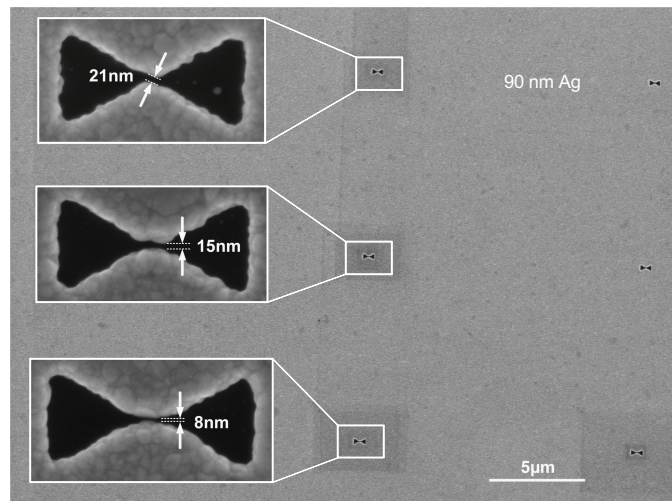
Figure 2.6: The bowtie apertures fabricated in 90 nm thick silver film. The smallest gap we can achieve is 8 nm.

bowties is lower.

2.3   Transmission Measurements

The optical properties of fabricated bowtie apertures were first characterized with a standard optical microscope in transmission mode (Leica DMRX). Light from the halogen lamp is passed through a polarizer to align the polarization across the gap. As seen in the color image in Figure 2.10 (a), different apertures transmit different colors of light in the visible wavelength range. The resonant transmission can be attributed to low-Q Fabry-Perot modes supported by the aperture terminated by air on one side and silicon nitride membrane on the other side. To quantify these resonances, transmission spectra were measured in a home-built setup (Figure 2.7) using a spectrometer (Horiba iHR550 with Synapse CCD array). A broadband light source spanning 440 to 900 nm was generated by a halogen lamp (Figure 2.8), and a polarizer was used to orient the polarization across the gap. A 0.8 NA objective ($\sim$ 1 um collection spot size) was used to collect the transmission from individual apertures. This transmitted light was coupled to a fiber which was sent to either an avalanche photodiode (APD) or spectrometer. A piezo stage was used to precisely position the aperture on the collection focal spot as measured by the APD. Transmission data were normalized to the spectrum obtained with the sample removed. The 150 nm thick silver film transmits >25 times less power than the aperture, so we do not expect direct silver
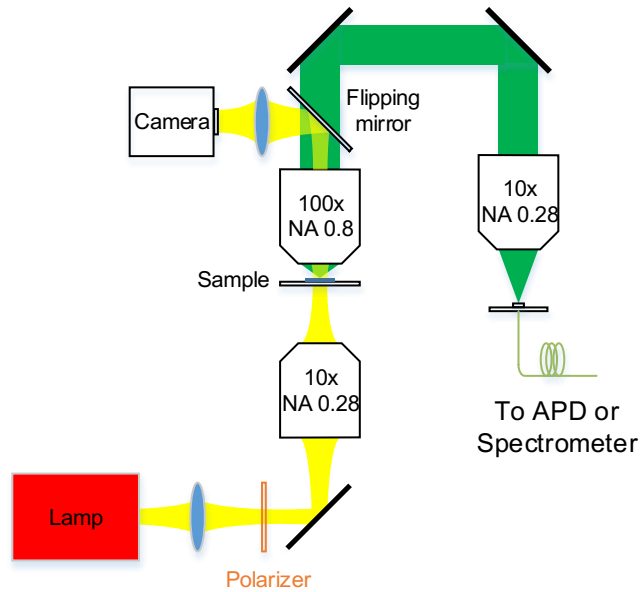
Figure 2.7: Schematic of apparatus for measuring the transmission of bowtie apertures.

transmission to influence the spectra shown below.

The most direct way to tune resonance wavelength is to change the silver film thickness, thus changing the length of the Fabry-Perot-like cavity. However, for a given sample, the film thickness is fixed, so here we demonstrated resonance tuning via control of the lateral gap dimensions of the aperture. The bowtie waveguide mode index (Figure 2.9) decreases with decreasing L and increasing G, causing resonance blue shift. Figure 2.10 (a) shows the transmission optical microscope image of a bowtie array in which we sweep G and L. In horizontal direction, from left to right, we increased the gap size G. In vertical direction, from bottom to top, we decreased the gap length L, which due to the nature of EBL also increases the gap size (Figure 2.1 (b), 2.10 (c)-(d)), as discussed above. The used EBL dosage
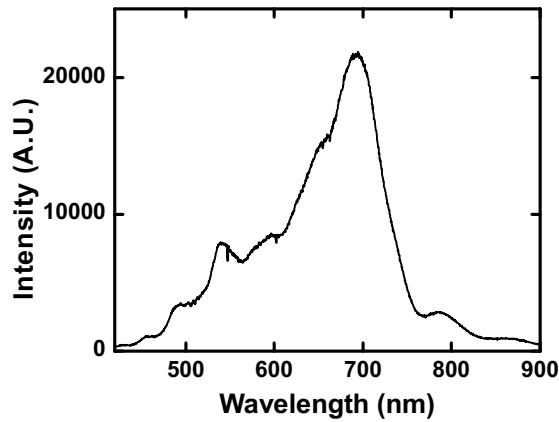
Figure 2.8: The spectrum of the halogen lamp light source, which is peaked around 700 nm.

is 3360 μC/cm². As shown in the optical image (Figure 2.10 (a)), the aperture color is blue-shifted toward the top-right (small L and large G). This array also demonstrates the high yield production capability of our fabrication technique. Figure 2.10 (e) shows the experimental transmission spectra of the apertures circled in (a), and quantitatively demonstrate resonance tuning from 684 nm to 565 nm. The smallest-gap bowtie we can fabricate is 11 nm. We also simulated the transmission spectra of these five apertures and the results match well. The detailed simulation method is described in the later paragraph. Also more experimental example of gradual resonance tuning in aperture array is shown in Figure 2.11.

To further increase the resonance tuning range, we also fabricated bowtie devices with a smaller outline. The smaller outline will tune the resonance towards shorter wavelength, without increasing the gap and thus sacrificing the enhancement. Figure 2.12 (a)-(c) show
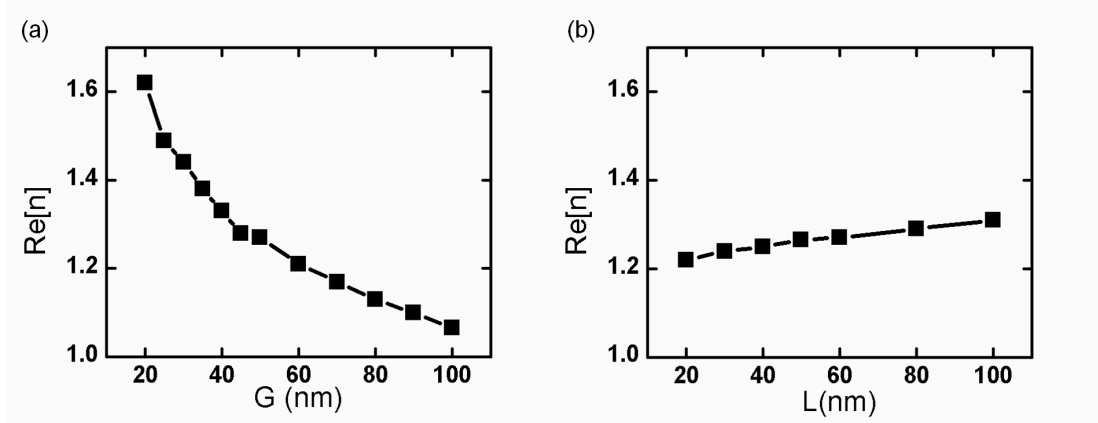
Figure 2.9: (a) Calculated mode index versus gap size G while L is fixed at 50 nm. (b) Mode index versus L while G is fixed at 50 nm. The index is calculated in infinitely long aperture waveguide, and the wavelength is set to be 700 nm. It shows that we can engineer the resonance by adjusting the bowtie dimensions.

the SEM images of three smaller bowtie apertures along with their color recorded with the transmission microscope. The measured transmission spectra show resonances at 470, 539, and 605 nm for the three apertures, which match the blue, cyan, and orange color, respectively, measured using the transmission microscope. Notice that Figure 2.12(b) and 2.10(b) have similar resonance wavelengths, but 2.12(b) has smaller gap and thus higher field enhancement due to smaller outline design. Despite the rough granular boundaries of the apertures, the resonances show quality factors larger than 6. The smallest aperture has the highest quality factor of all the measured devices at 11.8. However, it is also the dimmest among the three due to the smallest overall size.
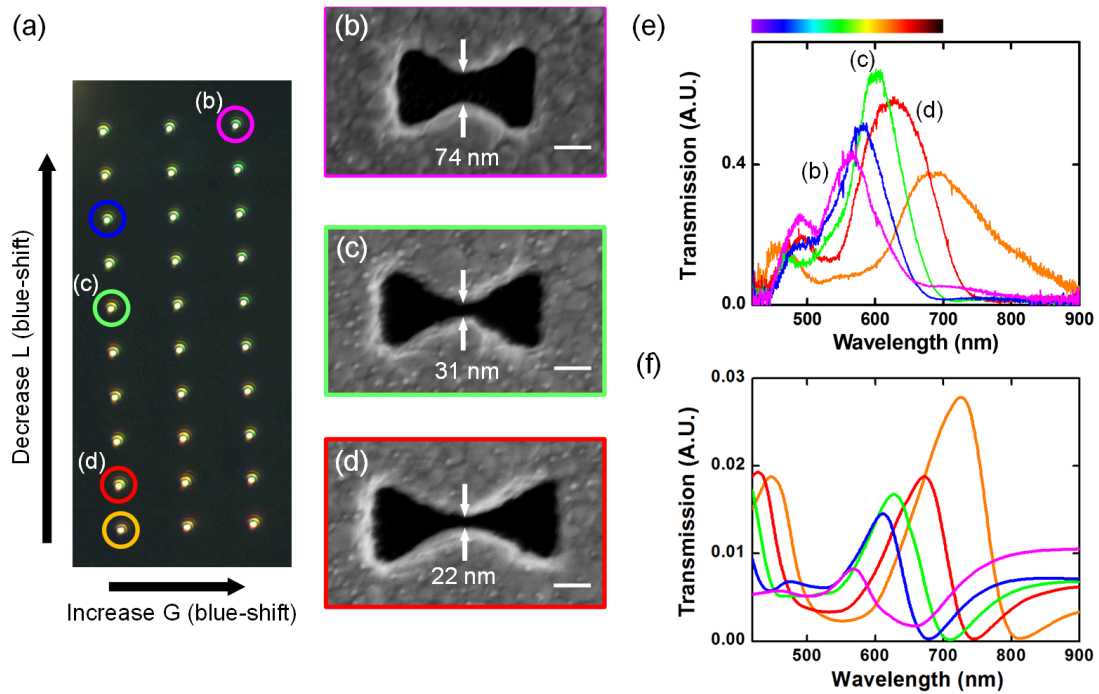
Figure 2.10: (a) The transmission optical image of the bowtie array fabricated in 150 nm thick silver layer: gap size G changes with column, and gap length L changes with row. Both decreasing L and increasing G will make the resonance blue-shifted. This array shows that the aperture resonance can be tuned smoothly via changing the lateral gap dimensions. Notice that the perceived color has a yellow hue due to the yellow halogen lamp light source used in this experiment. (b-d) SEM images of three measured bowtie nanoresonators in (a). The SEM image of the orange circled aperture is shown in Fig. 2.1(b). The e-beam dosage is 3360 μC/cm², and the scale bars are all 100 nm. (e) The transmission spectrum of five representative apertures circled in (a), normalized by the emission spectrum of the source. The resonance can be tuned continuously from 565 to 684 nm. (f) The simulated transmission of the five apertures with walls slanted at 20 degrees and rounded top corners with 75 nm radius of curvature in the model. It shows good agreement with the experiments. The colors used in the spectra lines correspond to the circle colors in (a).

(a)

Decrease L (blue-shift)

Increase G (blue-shift)

(b)
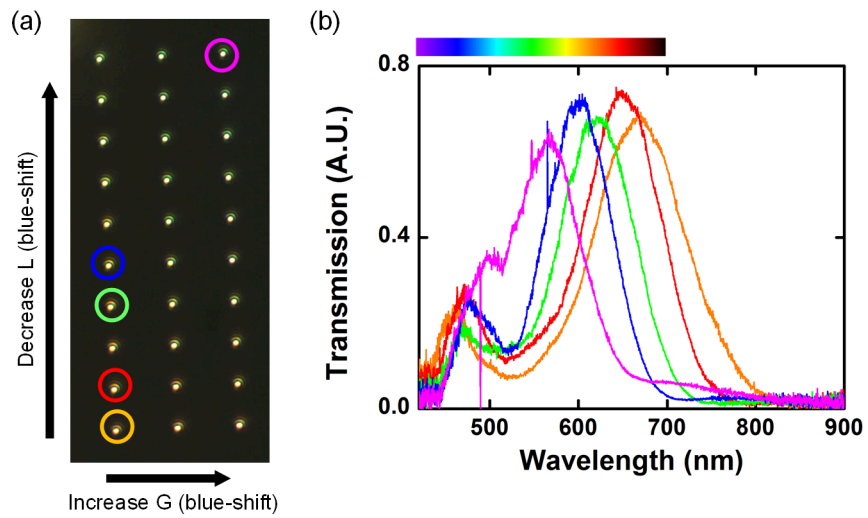
Figure 2.11: Another array example showing the gradual tuning: The apertures here are fabricated with 4128 μC/cm^2 e-beam dosage, which is higher than the ones shown in Figure 2.10 (a) The transmission optical image of the bowtie array. Both decreasing L and increasing G will make the resonance blue-shifted, so the color is blue-shifted toward the top-right. (b) The transmission spectrum of five representative apertures circled in (a), normalized by the emission spectrum of the source. The resonance can be tuned continuously from 566 to 668 nm. The colors used in the spectrum lines correspond to the circle colors in (a).
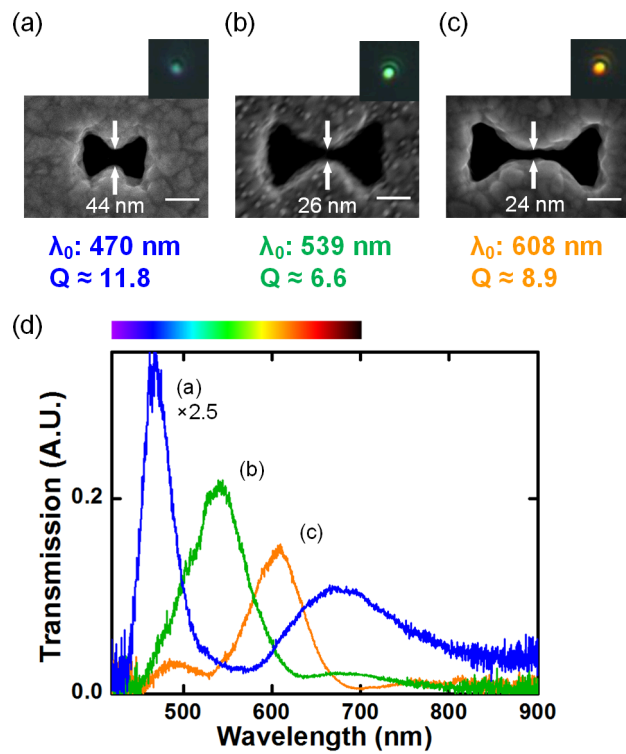
Figure 2.12: Resonances can be tuned further blue-shifted by shrinking the overall bowtie outline. (a-c) The SEM images of the three measured bowtie nanoresonators. On top right of each image is the optical image under the transmission optical microscope, showing the color of blue, cyan, and orange. The silver thickness is 150 nm, and the scale bars are all 100 nm. (d) The measured transmission spectra of the three apertures, normalized by the emission spectrum of the source. They correspond to the optical images well. The blue resonance has the highest Q factor, which is 11.8.

Q factors we measured are typically 6-8, and are near an order of magnitude smaller than

the theoretically predicted material Q of 40-60 in this wavelength range[48]. This suggests

our devices' Q factors are mainly limited by the sidewall tapering, surface imperfection,

and the radiation loss at the aperture interfaces. From the above SEM images, we can see

that the bowtie shape is well-defined by the modified lift-off after e-beam writing posts.

However, from Figure 2.13, it is clear that the boundary of the aperture is mainly defined by

large grains, and the surface is not smooth, which is likely a main contributor to the low Q

factors. Additionally, the sidewall of the aperture is slightly angled since during the evap-

oration step the silver layer deposited on top of the resist post grows laterally and creates

an umbrella effect which blocks the silver depositing on the SiN substrate. We performed

SEM imaging at a tilted angle, which showed the wall is slanted by 20-28 degrees for sev-

eral apertures (Figure 2.14). This issue could be solved by performing silver deposition on

a tilted and rotating stage. More vertical sidewalls would likely improve quality factors

by creating a more consistent mode propagating through the aperture. The more vertical

sidewalls give more abrupt changes at the interfaces, leading to higher reflections and thus

higher Q.

   We also simulated the transmission spectra of our apertures using a 3-D FDTD algo-

rithm (Lumerical Solutions, Inc.). The aperture geometry was characterized using scanning
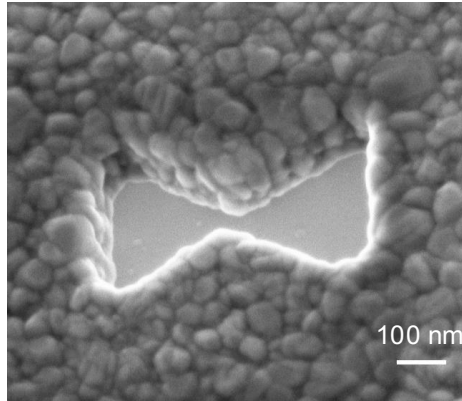
Figure 2.13: The aperture imaged with a tilted angle, showing the boundary is mainly defined by granular silver film.

electron microscope, and SEM images were imported into the simulation program, assuming the sidewalls are vertical. Dielectric properties of the silver film were directly measured via ellipsometry (J.A. Woollam), and we found it is slightly different from the literature [2,3,4] (Figure 2.15). Nevertheless, we found that the material properties have insignificant effect on the aperture resonances. In results, the simulation peak transmission wavelengths differ quantitatively from experimental results but reproduce the qualitative trend seen in the data: decreasing L or increasing G leads to blue. The simulation results are all red-shifted from the experiment ones. With the vertical cross section field plot, we confirmed the resonance is a Fabry-Perot like resonance with one node inside (left part of Figure 2.16). We attribute the quantitative inaccuracy to the tapering of our apertures. To investigate this possibility, we used the bowtie model shown in Figure 2.1(a) to approximate the imaged

23

(a)   (b)

22 nm

21 nm
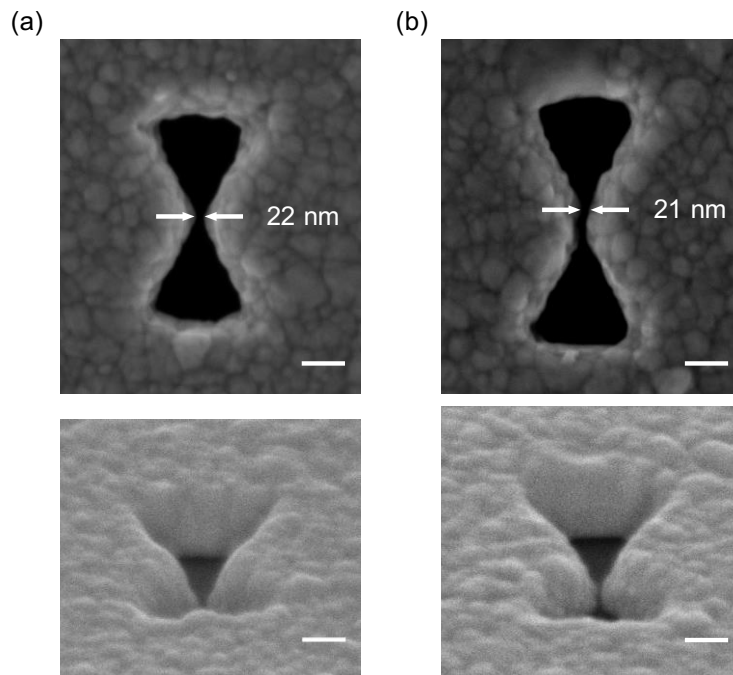
Figure 2.14: (a) (b) Vertical top-view SEM images of two example apertures and their corresponding tilted SEM images. The imaging stage was tilted at 60 deg from vertical. We can see the walls of the apertures are slanted with rounded top corners. We calculate the wall is slanted by 20 to 28 degrees for all the imaged apertures. All the scale bars are 100 nm.

bowtie apertures and tapered the sidewall. We assume the sidewalls are slanted by 20 degrees and the top corners are rounded in order to model the aperture geometry more accurately. After modifying these two factors, we can see the simulations match experiments better, suggesting these factors contribute to the remaining discrepancy (Figure 2.10(f), and right part of Figure 2.16(c)). When the sidewalls are slanted, the overall gaps become bigger. As we mentioned earlier, increasing G makes the resonances blue-shifted due to the decreased mode index. The new blue-shifted simulations results match better with the experimental results.

2.5 Conclusion

In summary, using EBL and modified lift-off we have fabricated small-gap bowtie metal apertures, with gap dimensions as small as $\sim$ 11 nm, which have previously been fabricated using more time consuming FIB milling processes. The ability to do large-scale fabrication enables high throughput cavity design optimization and experimentation. Transmission spectra confirm the resonators' resonances and demonstrate Q factors as high as 11.8. The bowtie apertures presented here offer an exciting platform for applications in light-matter interaction engineering, optical tweezing, and surface-enhanced Raman scattering. Thus they may have applications in coupling to quantum emitters like defect centers in diamond[49] or quantum dots[50]. Use of these apertures to trap and pump colloidal quantum
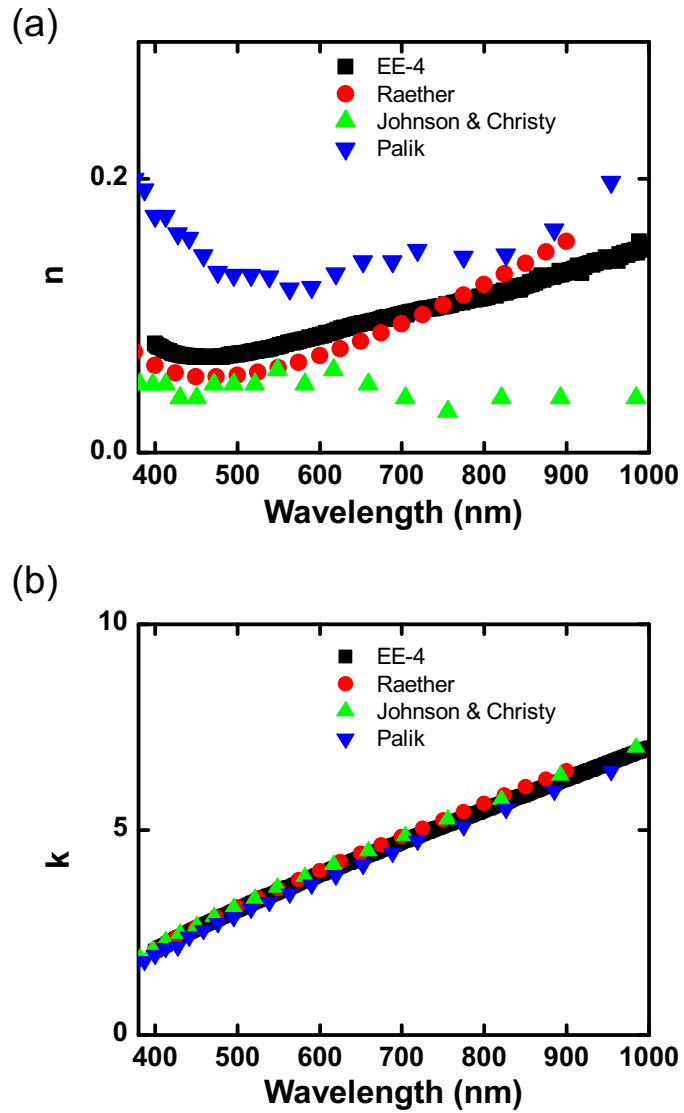
Figure 2.15: (a) (b) The real and imaginary part of the refractive index of silver in 400 - 1000 nm [2,3,4]. The data by Raether is closer to our measured one.
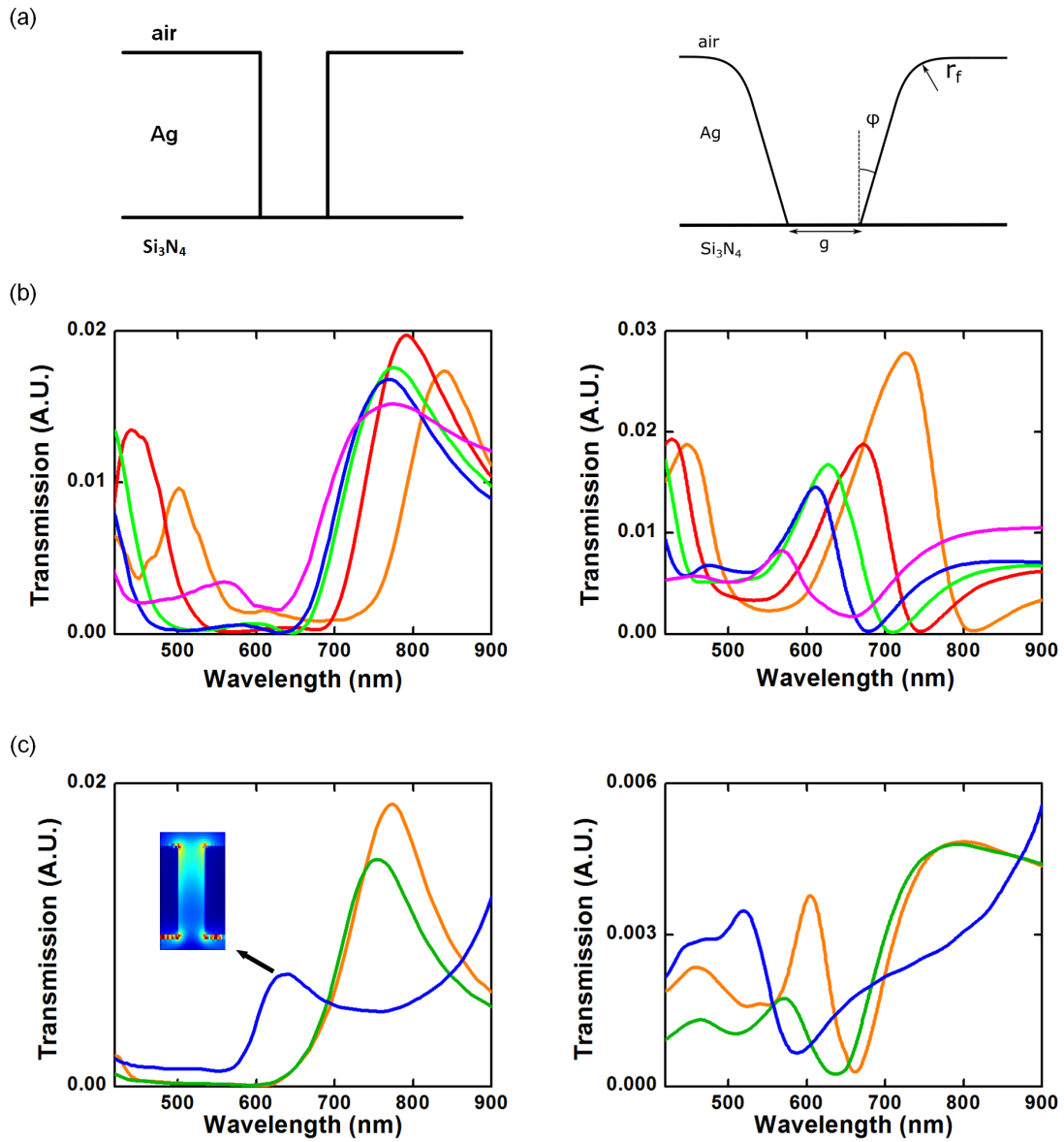
Figure 2.16: (a) Schematics of two different types of simulations: the left figure assumes vertical wall and sharp top corners, while the right figure has slanted wall and rounded corners. In the simulations we used 20°for the slant angle φ and 75 nm for radius of curvature r_f. (b) The simulation results of the five apertures in Figure 2.10 with vertical (left) and slanted-curved (right) wall. (c) The simulation results of the three apertures in Figure 2.12 with vertical (left) and slanted-curved (right) wall. The field profile inset shows that the resonance is a Fabry-Perot like resonance with one node inside. The colors used here are the same as the ones in Figure 2.10 and 2.12. We can see that with slanted walls and rounded top corners, the simulation results are improved and match better with the experimental results.

dots with two-photon excitation has already been demonstrated[29]. Finally, with ultrasmall

mode area and clear colors, these apertures may find use as ultrasmall color pixels[51].

3

Optical Trapping of Colloidal Quantum

Dots using Bowtie Apertures

In this chapter, bowtie apertures were used to trap single silica coated quantum dots (scQD) with a diameter of 30 nm with a trapping laser intensity of 1.56 MW/cm² at 1064 nm. Because of the strong field confinement inside the bowtie aperture, 640 nm scQD emission

was detected following two-photon excitation by the 1064 nm trapping laser. The enhanced two-photon excitation eliminates the need for a separate excitation source and results in a system that self reports via emission when trapping is achieved. We show simulations to evaluate theoretical trapping performance and experimental examples of single scQD trapping with simultaneously recorded laser transmission and emission.

3.1   MOTIVATION - DETECT SINGLE QUANTUM DOT ABSORPTION SPECTRUM

The study of fundamental properties (i.e. lifetime, polarization) of single emitters, such as colloidal quantum dots, has mostly relied on spectroscopy techniques based on emission. Meanwhile, the mechanisms for certain single emitter behaviors including blinking[6], spectral and temporal diffusion[5], are not fully understood, and can potentially benefit from a direct measurement of the electronic structure via broadband absorption spectroscopy. The single dot absorption spectroscopy was performed with scanning laser on the self-assembled quantum dots[52]. However the inhomogeneity, linewidth and spectral diffusion of the colloidal quantum dots might be larger than the self-assembled ones. So we proposed to use the broadband light source and measure the difference of transmission spectra with and without the dot. This method will enable us to measure more broadband absorption spectra and have higher throughput. However, the challenge in measuring single emitter absorption lies in the small absorption cross section in comparison to a diffrac-

(a)

(b)
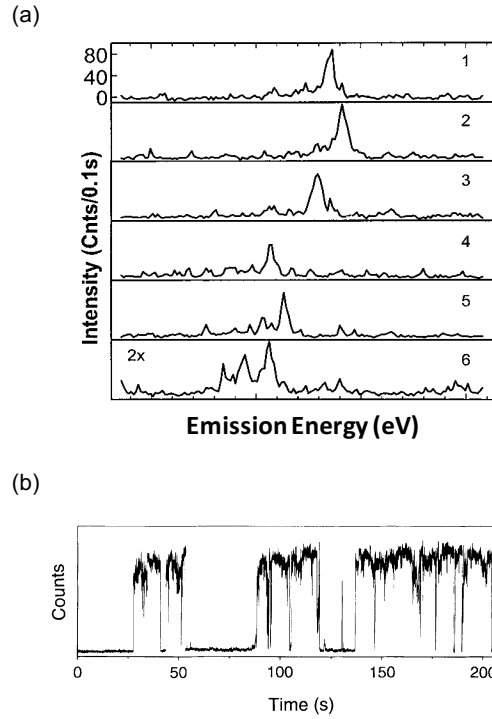
Figure 3.1: (a) Quantum dots spectral diffusion. The emitted photon wavelength fluctuates over time[5]. (b) Blinking behavior of quantum dots[6].

tion limited optical beam, which leads to a small absorption probability.

The absorption probability of a single quantum emitter can be expressed as a ratio between its cross section and mode area of the confined light, which can be written as:

$$A_{\text{mode}}(x_{\text{o}}, y_{\text{o}}) = \iint \Re\left[\frac{\partial \omega \varepsilon(x, y)}{\partial \omega}|E(x, y)|^2\right] dxdy \bigg/ \Re\left[\frac{\partial \omega \varepsilon(x_{\text{o}}, y_{\text{o}})}{\partial \omega}|E(x_{\text{o}}, y_{\text{o}})|^2\right] \quad (3.1)$$

free space focusing   **plasmonic apertures**

broadband light source   broadband light source
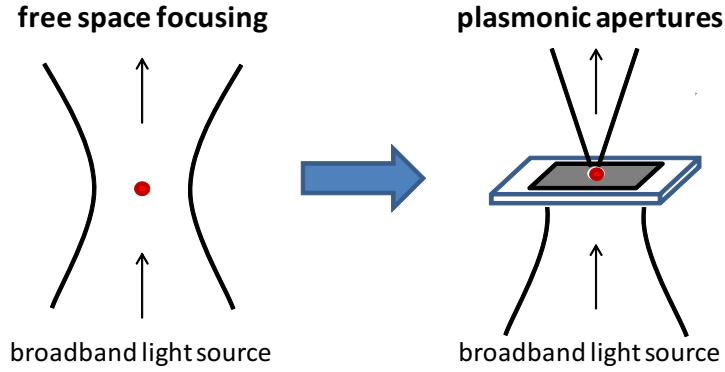
Figure 3.2: The proposed plasmonic apertures will force the light couple to its waveguide mode with smaller mode area. Thus the absorption probability will be enhanced.

$$Probability = \frac{\sigma_{\text{abs}}}{A_{\text{mode}}(x_\circ, y_\circ)} \tag{3.2}$$

$(x_\circ, y_\circ)$ is the position of the emitter, and σ_{abs} is the absorption cross section of the quantum dot (QD). Because colloidal quantum dots usually are weak dipoles, we regard our CdSe/Zns QDs having tiny absorption cross sections of 1 nm². When placed in tightly focused beam with focal spot size of $\sim$1 μm², photon absorption probability is as low as 10^{-6}. This makes it difficult to perform the absorption spectroscopy of the QD.

A plasmonic aperture, formed by a subwavelength hole in a metal film, allows for strong confinement of optical fields due to the excitation of localized surface plasmons and can be used to enhance light-matter interaction, such as absorption, so that light transmission through the aperture can be used to extract the absorption spectrum of a single quantum

dot.

The figure of merit here is the mode area, which describes the energy confinement in the structure, since the absorption probability between an incident photon and the dot is the ratio between the absorption cross section and the mode area for an optimally placed emitter. We started from a circular aperture and solved for the optical modes inside the air-silver aperture as a function of radius using Maxwell's equations and verified our analytical data using FDTD simulations. The QD we use for our modeling has an absorption edge at around 640 nm. We found that the fundamental guided HE11 mode dominates in our fabricated apertures[46]. The calculated mode area for a 50nm-radius Ag aperture is around $0.06(\lambda/n)^2$ and thus the absorption probability is 4.4×10^{-5} (assuming the absorption cross section is around $1nm^2$, and the QD is placed in the center of the aperture) (Figure 3.3). However, unlike the electric field, simulations show that the energy density is mainly focused in the silver rather than air, which decreases the interaction between the QD placed in air and the light field. To better confine light in the air region, other types of plasmonic structure such as coaxial[21], crescent[53], bow-tie[54] apertures, might be more suitable.

Here we propose to use bowtie aperture to achieve small mode area due to the successful fabrication of them. The energy density is fairly uniform inside the gap, unlike the circular aperture. We calculate the mode area by assuming the QD is located at the center of the gap. Notice that the mode area would be even smaller if the QD is closer to the tips,
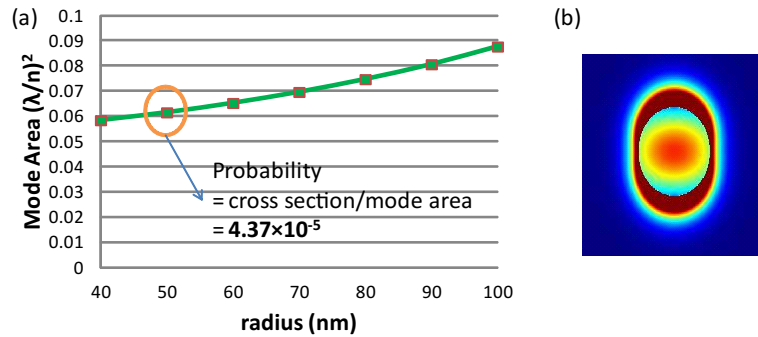
Figure 3.3: (a) Mode area of the circular aperture versus radius, showing that our aperture could reach a mode area of $0.06(\lambda/n)^2$ and thus an absorption probability of 4.4×10^{-5}. (b) Energy intensity in a 50 nm circular aperture (rescaled). It shows that the energy is mainly concentrated in the metal in the circular case.

where the field intensity is maximum (Fig. 3.4(a)). Simulations show that the mode area is proportional to the gap size and is less dependent on the gap length (Fig. 3.4(b)). With the reasonable fabrication, the mode area can be roughly two orders higher than that in the standard optical transmission spectroscopy, suggesting that this device may be suitable for single molecule detection. Notice that in chapter 2, with state of the art fabrication, we can fabricate 10 nm gap bowtie aperture, which has only 0.002 $(\lambda/n)^2$, giving the possible 3 orders of magnitude improvement. Besides, in low temperature, the probability could be increased by 1 order due to the decreased linewidth, and the absorption signal could be observed given our experimental apparatus.

We placed dots into the apertures by dropcasting and obtained ensemble quantum dot absorption spectra like Figure 3.5. It is hard to control the number of the dots inside the
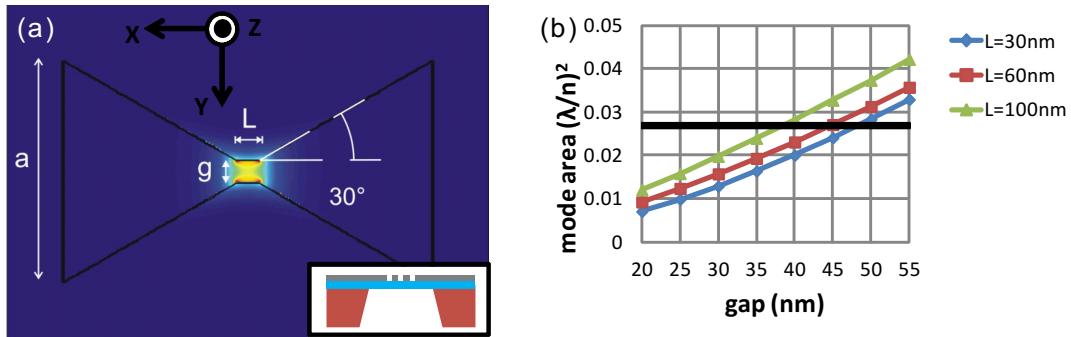
Figure 3.4: (a) The schematic of the designed bowtie and the fundamental gap mode energy density distribution. g is gap width, L is gap length, side length a = 300 nm. Inset: the side way of the sample (not to scale), with bow-tie aperture defined in top silver layer. (b) The mode area versus gap size in different gap length. The black line is the mode area which creates 10^{-4} absorption probability.

aperture, and ideally we want exactly one dot inside the aperture. Also, after the dropcasting the aperture cannot be reused again for the experiment. We need lots of single dot absorption spectrum measurements in order to quantify the blinking, spectral diffusion, and inhomogeneity. Here we proposed using optical trapping to mitigate this problem. The optical trapping enable us to trap single QD inside the aperture. Also, by toggling the trapping beam, the measured QD is released and a new QD can be trapped for another measurements. The measurements of lots of QDs can be achieved using the optical trapping.

3.2 Introduction of Optical Trapping

Optical tweezers have been a powerful tool to fix, control, and manipulate small objects[55]. The introduction of plasmonic structures has further greatly advanced the field of opti-

cal trapping in the last decade. These structures provide enhanced, localized electric fields that require lower incident flux and can trap smaller particles when compared to free space trapping[56,57,58,59,60,61]. Trapping is further enhanced in plasmonic apertures by self-induced back-action (SIBA)[16], a positive feedback mechanism that increases the trapping force due to dielectic loading of the aperture when a particle is trapped. Recently, there have been many plasmonic nanoapertures designed for trapping particles as small as tens of nanometers. Trapping with plasmonic apertures has been performed with circular[16] and rectangular apertures[62]. Introducing a pinch point into the aperture, people used double nanoholes to trap a 12 nm silica bead[17], while others fabricated bowtie apertures on films and on fiber tips to implement 20 nm polystyrene bead trapping and 50 nm bead manipulation[28]. The opposing prongs at the pinch point of the aperture act as dual sharp tips to greatly enhance electric fields in the gap[63], giving rise to a localized field gradient suitable for optical trapping. This confined fundamental gap mode has also been used to provide a narrower near-field pattern for lithography[33], higher throughput near-field scanning optical microscopy[64], and enhanced molecule fluorescence[31].

Various types of particles have been used in optical trapping studies, including gold nanoparticles[65], nanorods[66,67,68], globular proteins[69], single-cell organisms[70,58], polystyrene spheres with[28] and without emissive dye[17], and colloidal quantum dots (QDs)[71,72]. Colloidal quantum dots (QDs) are attractive candidates for optical trapping and simultaneous

electronic excitation because their high index of refraction[73] increases the trapping force, and their broad continuum of excited states makes them strong absorbers[74,75].

Colloidal QDs have exciting applications in biomolecule labeling due to a high photo-bleaching threshold, good chemical stability, and tunable spectral properties. The ability to optically manipulate QDs may help in fluorescent marker placement and molecular force measurements, but fluxes required for optical trapping[71] and non-linear excitation[72,76] in free space are large and may be harmful to biological samples. Plasmonics can help to decrease the required trapping power, but trapping with a plasmonic structure generally renders QDs non-emissive due to interactions with the nearby metal[77,78].

In this work, these issues were solved by trapping silica coated quantum dots (scQDs) using bowtie apertures in a silver film. The bowtie apertures facilitated optical trapping and two-photon excitation such that the required flux was over one order of magnitude lower than previously reported for trapping in free space[72], and the silica coating insulated the QDs from the metal to mitigate quenching. The larger size of the scQD also makes the trapping easier. Also, the bowtie apertures were fabricated by e-beam lithography followed by lift-off rather than the past conventional focused ion beam milling procedure to provide larger aperture quantities for higher throughput device testing.

3.3   Silica Coated Quantum Dot (scQD) Synthesis and Characterization

Core/shell CdSe/CdS colloidal quantum dots (QDs) were synthesized as previously described[79,80]. Silica overcoating was performed by loading 30 mL anhydrous cyclohexane into a 100 mL round bottom flask. Under vigorous stirring, 4.75 mL of Igepal CO-520 was added. After stirring for 10 minutes, 1 mL of QD-cyclohexane solution (3 μM) was injected into the reaction followed by slowly adding 150 μL tetraethyl orthosilicate (TEOS, 99%). After another 10 minutes of stirring, 0.5 mL of ammonium hydroxide solution (28% in water) was injected dropwise into the solution. The final reaction solution was stirred for 18 hr at room temperature before purifying the scQDs via precipitation using ethanol ($\sim$20 mL) and collecting by centrifugation. The scQDs were washed with ethanol twice more and finally dissolved into 2 mL DI-water before storage at 4 until use. Normalized absorption and emission spectra are shown in figure 3.5.

Prior to some measurements, the scQD solution was passed through a 20 nm pore syringe filter (Whatman) to reduce the mean particle diameter. Dynamic light scattering (DLS) was performed on filtered and unfiltered particles and results calculated by volume are plotted in Figure 3.6. Mean hydrodynamic diameters are 21.1 nm and 39.2 nm for filtered and unfiltered particles, respectively. It should be noted that because DLS measures the hydrodynamic diameter of particles, these results are likely an overestimation of the actual particle sizes.
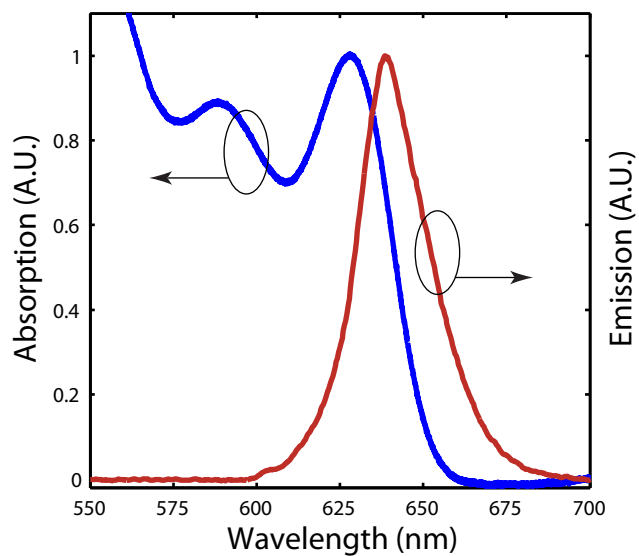
Figure 3.5: Normalized absorption (blue) and emission (red) spectra for scQDs. Continuous wave 532 nm excitation was used as an excitation source for the emission spectrum.
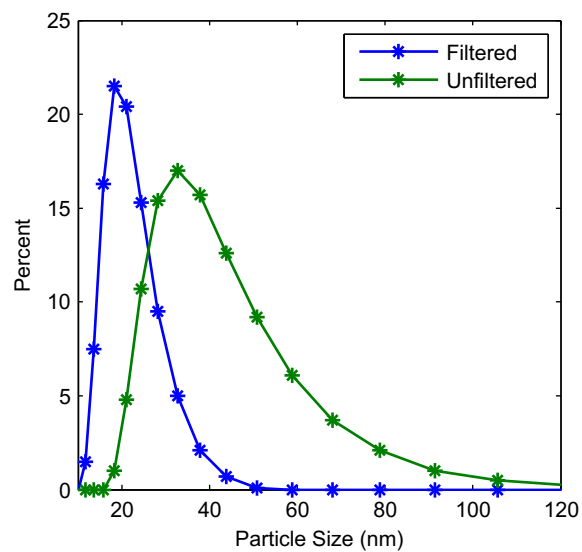
Figure 3.6: Size distribution of scQDs before (green) and after (blue) filtering measured with DLS. Sizes were calculated by volume.

Scanning electron microscope (SEM) images of the apertures used in the experiments are shown in figure 3.8a and 3.8b overlapped with simulated field intensity enhancements. The dominant gap mode is supported by the aperture when the trapping beam polarization is oriented across the gap. Enhancement is a unitless factor that scales the intensity in the gap relative to the free space intensity. Both apertures, with gaps of 38 nm and 56 nm, were used to successfully trap scQDs. Given that the field enhancement is lower in the 56 nm gap aperture, the required trapping laser intensity is higher and the calculated trapping potential suggests it should only be able to trap larger particles. The aperture is realized on an underlying silicon nitride (SiN) membrane (thickness 100 nm) and is immersed in water. A 3D sketch of our device trapping quantum dot is illustrated in figure 3.7. In this way the aperture forms a low-Q Fabry-Perot cavity whose resonance can be tuned by silver film thickness[44]. A 130 nm thick silver film was used to achieve resonances centered at 850 nm and 915 nm (Fig. 3.8c), thus satisfying the requirement imposed by the SIBA[16] mechanism for a peak transmission resonance slightly blue-shifted from the trapping laser. A transmission electron microscope (TEM) image of the scQDs used in trapping shows particles with a CdSe/CdS core/shell[80,79] center and total sizes that are $\sim$ 30 nm in diameter (Fig. 3.8d), with a mean hydrodynamic diameter of 39.2 nm as measured by dynamic light scattering (Figure 3.6). Procedures for the fabrication of the bowtie apertures are provided in the pre-
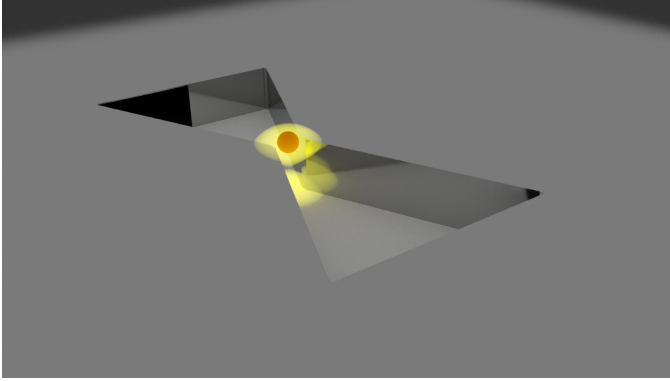
Figure 3.7: 3D schematic of our bowtie aperture.

vious chapter.

3.5 Trapping Potential Simulation Using Maxwell Stress Tensor

It was shown in simulations that bowtie antennas might be able to trap quantum dot, with the pumping wavelength near the resonance of the QD to create a larger dipole for easier trapping[81]. In order to quantify and evaluate the trapping capability of the apertures, finite-difference time-domain (FDTD) simulations (Lumerical Solutions, Inc.) were performed. Maxwell Stress Tensor (MST) was used to calculate the trapping force and then the force was integrated to get the trapping potential (Fig. 3.10). The optical force exerted on the particle can be obtained by integrating the inner product of tensor and surface unit vector $\vec{n}$ over the volume encompassing the particle:

$$\langle \vec{F} \rangle = \int_{\partial V} \langle \overleftrightarrow{T}(\vec{r}, t) \rangle \cdot \vec{n}(\vec{r}) \, da \tag{3.3}$$
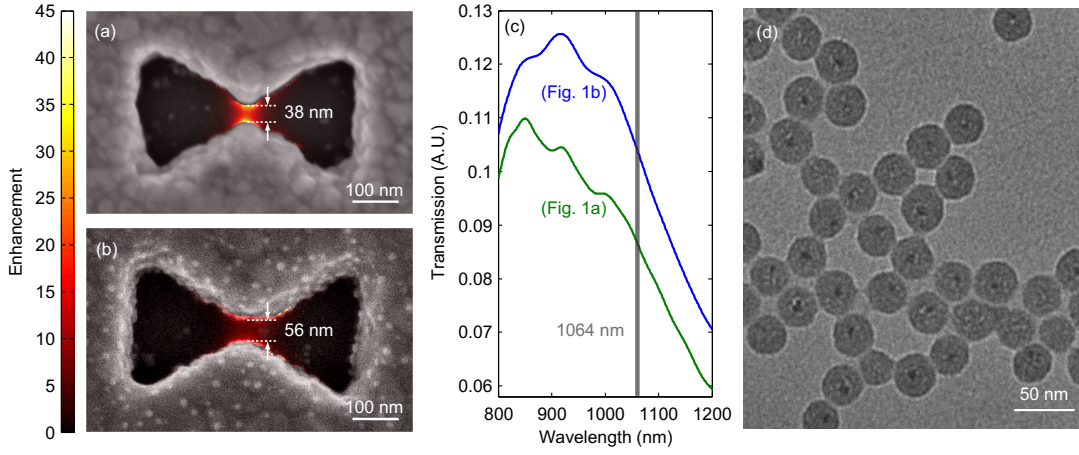
Figure 3.8: (a)(b) SEM images of the bowtie apertures used in the experiments, overlapped with field intensity enhancement profiles at 1064 nm. The confined gap mode is dominant when the polarization is across the gap. (c) The simulated transmission spectra of the two apertures used in trapping experiments, showing peak resonances are blue-shifted from the 1064 nm trapping laser. (d) Transmission electron microscope image of the silica coated quantum dots used in trapping.

where the Maxwell Stress Tensor $\overleftrightarrow{T}$ is defined as:

$$\overleftrightarrow{T} = \varepsilon_o \vec{E} \otimes \vec{E} + \mu_o \vec{H} \otimes \vec{H} - \frac{1}{2}(\varepsilon_o E^2 + \mu_o H^2)\overleftrightarrow{I} \tag{3.4}$$

Here $\otimes$ is the outer product and $\overleftrightarrow{I}$ is the unit tensor. MST gives us the completely rigorous calculation of force when QD is at one position. The integration over the surface should be exactly correct. However for the sake of less numerical error, we chose the so called volumetric method suggest by Lumerical. It comes from Lorentz force law, which is

exactly the origin of MST:

$$\vec{F} = \varrho\vec{E} + \varrho\vec{v} \times \vec{B} = \varrho\vec{E} + \vec{J} \times \vec{B} \tag{3.5}$$

where ϱ is the charge per unit volume and J is the current density:

$$\varrho = \varepsilon_{\circ}\nabla \cdot \vec{E}, \vec{J} = -\frac{\partial P}{\partial t} \tag{3.6}$$

Thus the optical force becomes:

$$\vec{F} = \varepsilon_{\circ}(\nabla \cdot \vec{E})\vec{E} + i\omega\vec{P} \times \vec{B} = \varepsilon_{\circ}(\nabla \cdot \vec{E})\vec{E} + i\omega(\varepsilon - \varepsilon_{\circ})\vec{E} \times \vec{B} \tag{3.7}$$

We integrate the force calculated here over the whole space encompassing the particle, and then the integrated force is exactly the optical force exerted on the particle. This volumetric method provides better numerical accuracy especially when the particle is close to the boundary of integration volume.

Simulations were first performed on the 38 nm gap aperture (Fig. 3.8a) with the incident trapping beam focused on the entrance of aperture. The scQD was simulated as a 6nm CdSe core with silica coatings of varying thickness to produce final diameters of 20 nm, 25 nm, and 30 nm, and was placed close to the silver wall to get the strongest trapping poten-
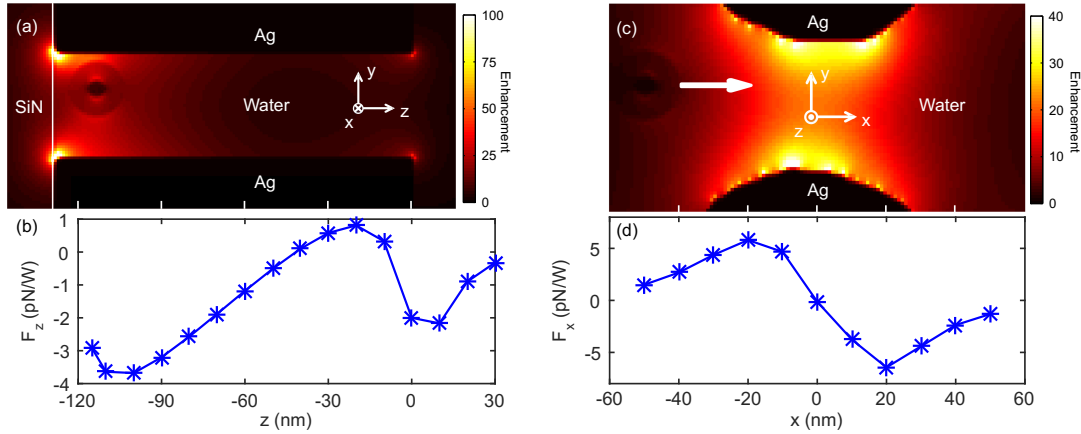
Figure 3.9: (a) The intensity enhancement and (b) force along the z axis. (c) The intensity enhancement and (d) force along the x axis. All forces are normalized to input power.

tial possible. The field intensity before entering the aperture was recorded, scaled to the experimental incident flux of 1.56 MW/cm², and used to calculate trapping force and potential. Figure 3.9 shows the calculated optical force and intensity enhancement experienced by a 20 nm scQD along z and x axes in the aperture. Note that the force is positive at -25 nm (Fig. 3.9b), pulling the particle towards the front surface of the aperture. We calculated the z axis trap stiffness of 0.07 fN/nm/mW using the range from -60 nm to -80 nm where the change in force is steepest. The calculated x axis trap stiffness is 0.42 fN/nm/mW, which are comparable to stiffness measured for similar double nanohole structures[82] and are nearly two orders of magnitude larger than in the case of free-space trapping[71,72]. The stiffness and force are larger along x axis because field is more confined in x-y plane.

Then, the force was integrated to get the potential. The calculated trapping potential exhibits two local minima due to field enhancement occurring on both faces of the aperture

from operating near the 1st-order Fabry-Perot resonance [44], with the deeper trapping potential at the water-SiN interface. Optical trapping is considered favorable when the trapping potential overcomes the ambient thermal energy $k_B T$ (T = 300 K), which was observed for particles of at least 25 nm in this system at the water-SiN interface. The trapping potential at the front surface of the aperture did not overcome $k_B T$, regardless of particle size. From the simulations mentioned above, we assumed that the trapped scQD is located at the bottom of aperture, touching the silicon nitride membrane and the apex of the bowtie. However, as discussed in the literature [83], it is possible that the QD could move around due to Brownian motion. Factors not accounted for in the simulations could potentially enable trapping particles smaller than 25 nm with this system. As the literature [77] suggested, van der Waals forces between the particle and the surrounding aperture surfaces could facilitate trapping when potentials do not overcome $k_B T$ of ambient thermal energy, and reduced degrees of freedom for particle motion inside the aperture should reduce the particle's kinetic energy, making escape from the aperture more difficult.

Figure 3.11 shows the calculated potential for the 56 nm aperture in manuscript Figure 3.8b. Figures 3.8a and 3.8b were patterned using the same design template, but they assumed different final dimensions due to dosage differences (3360 μC/cm² for Fig. 3.8a and 3648 μC/cm² for Fig. 3.8b) and fabrication variance. The 56 nm aperture exhibits the same dual minima characteristic as the calculated potential for the 38 nm aperture. Simulations
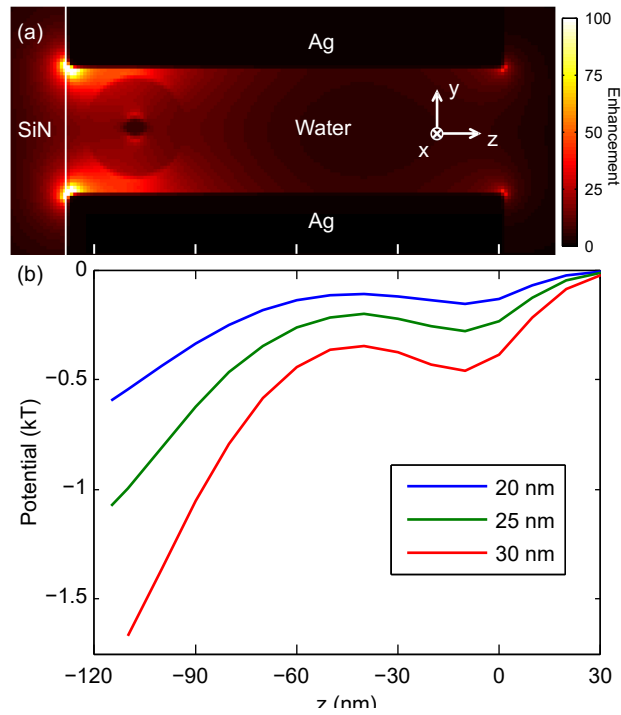
Figure 3.10: (a) The simulated field intensity distribution inside the aperture showing field enhancement on both faces of the aperture. The 30 nm scQD is shown in its final position at the bottom of the aperture touching the SiN membrane. (b) Potential energy calculation results showing that scQDs of at least 25 nm will have a potential lower than $-1\,k_B T$ at the bottom of the aperture.
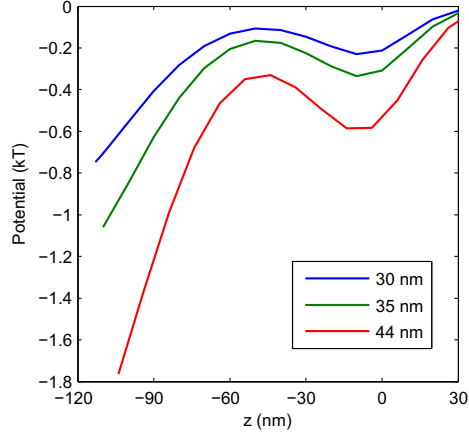
Figure 3.11: The calculated potential for particle trapping with the 56 nm aperture in manuscript figure 3.8(b).

show the minimum particle size this aperture can trap is 35 nm by overcoming $k_B T$ of ambient thermal energy. However, as discussed earlier, non-optical mechanisms such as van der Waals force and reduced particle degrees of freedom could enable trapping of smaller particles.

3.6 GRADIENT FORCE CALCULATION AND COMPARISON WITH MAXWELL STRESS TENSOR

In order to understand whether our device operated in SIBA regime or not, we also performed the simulations using the gradient force and scattering force formulation given by:

$$\langle \vec{F}_{\mathrm{grad}}(r) \rangle \approx \pi \varepsilon_e R^3 \frac{\varepsilon_p - \varepsilon_e}{\varepsilon_p + 2\varepsilon_e} \nabla |\vec{E}(r)|^2 \tag{3.8}$$

$$\langle \vec{F}_{\text{scat}}(r) \rangle \approx \frac{128\,\pi^5 R^6}{3\lambda^4 c} \frac{\varepsilon_p - \varepsilon_e}{\varepsilon_p + 2\varepsilon_e}^2 I_\circ(r)\vec{s} \tag{3.9}$$

where ε_p is the dielectric constant of the particle, ε_e the dielectric constant of the surrounding medium, R the radius of the particle, $I_\circ$ the trappling laser intensity, and $\vec{s}$ the unit vector of the propagation direction. The gradient force mainly pulls the particle toward to the focal spot, while the scattering force mainly pushes the particle out of the focus and towards the propagation direction. The optical trapping occurs when the gradient force dominates over the scattering force. These two formulas are conducted in the condition of assuming the particle can be approximated as a dipole without perturbing the surrounding electromagnetic wave. On the other hand, SIBA is the regime that trapped particle acts as an active role and will perturb the nearby electromagnetic wave, and thus the calculated forces from MST will differ a lot from the one calculated by gradient force[16]. By comparing it with the results using MST (Fig. 3.12), we can see with MST method the force is indeed larger, but the difference is really small, showing that our trapping is not close to SIBA regime yet. This proves that there is still space to improve our device trapping capability by making the particle take a more active role, and thus the required trapping power can be further decreased. The calculation show that the scattering force is 5 orders smaller than the gradient force, so we neglected it.
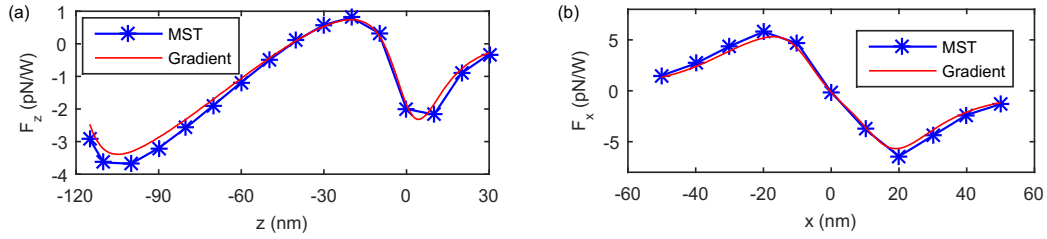
Figure 3.12: (a) (b) Comparison of the forces calculated by Maxwell Stress Tensor and Gradient force.

3.7 SETUP

Prior to trapping experiments, the aperture film was packaged with an aqueous scQD solution based on a procedure presented in the past literature[17]. A reservoir was made by cutting a 3 × 3 mm square from a 30 μm thick polydimethylsiloxane (PDMS) spacer on top of a 80 μm thick cover slip. Then a small drop of scQD solution (0.07% w/v) was placed in the reservoir and the aperture film was placed face down on top of the reservoir. A cross section of the sample packaging is shown in the inset of figure 3.13. We can see that our aperture device is surrounded by silver with size of 7.5 x 7.5 mm square. Its high thermal conductivity (429 W/m/K) should act as a good heat sink. This implies that our device temperature should not increase too much under the trapping laser illumination[60].

Optical trapping was achieved by transmitting a continuous wave (CW) 1064 nm trapping beam through an aperture packaged with scQDs as shown in figure 3.13. The optical quality of a 1064 nm trapping beam (Laser Quantum Ventus 1064) was cleaned with a polarizing filter and a 1064/10 nm laser line filter, expanded, and slightly defocused to correct

for chromatic aberration of the trapping objective. The trapping objective was a $100\times$ (1.25 NA) oil immersion objective that formed a spot radius of $1\,\mu$m with 1.56MW/cm^2 of incident flux at 1064 nm. Emission from trapped scQDs was collected with the same objective, separated from the 1064 nm trapping beam with a 900 nm short pass dichroic mirror, and sent to either a silicon avalanche photodiode (APD, Perkin Elmer SPCM -AQRH-13) or a spectrometer/CCD camera combination (Princeton Instruments Acton SP2750A/Pixis 1024) for detection of two-photon excitation upon trapping. Above the packaged film, 1064 nm transmission intensity through the aperture was collected with a $60\times$ (0.7 NA) air objective and sent to a Ge photodiode (Thorlabs DET50B) to monitor jumps in transmission intensity coinciding with trapping events. Sample positioning was achieved by a 3-axis stage (Thorlabs Nanomax-TS).

3.8   Optical Trapping of scQDs

Single scQD trapping in the 38 nm aperture using scQDs shown in figure 3.8 is demonstrated in figure 3.14 and is characterized by a stepwise increase in both emission and transmission intensities at 50 seconds. The stepwise increase in trapping laser transmission is due to dielectric loading of the particle. Intensity fluctuations are observed in the emission channel at $\sim$110 seconds followed by a gradual decrease in intensity. Corresponding dynamics in the transmission channel are absent or undetectably small, suggesting that scQD emis-
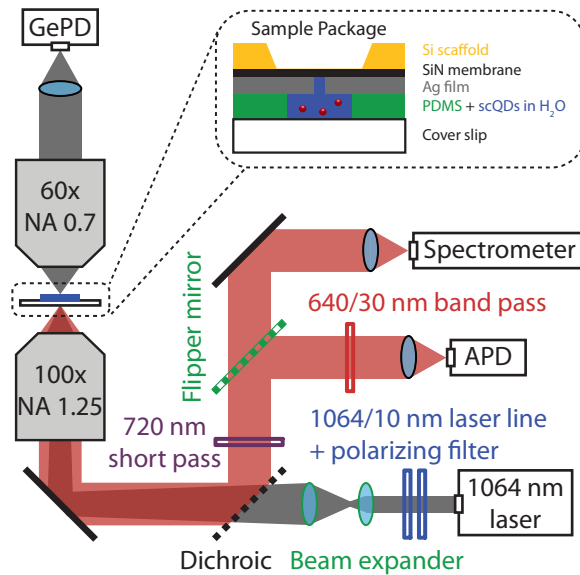
Figure 3.13: Instrument schematic for simultaneous trapping with 1064 nm laser (gray beam) and scQD emission detection at 640 nm (red beam). (Inset) Cross section of sample package.

sion dynamics (i.e. blinking, bleaching) may be responsible for the fluctuations observed in the emission channel. Alternatively, the emission channel may be far more sensitive to very small changes in particle position due to the nonlinear nature of two-photon excitation, resulting in large fluctuations in the emission channel accompanied by an increase in transmission channel noise. This might also explain the measured signals at 60 and 160 seconds: there is a small increase followed by gradual decrease in the emission intensity, with no observable change in the transmission intensity. We believe that this can be explained by scQD moving into and then out of the location with stronger excitation flux. A final possibility is that two particles were simultaneously trapped and emission ensued for the respective particles at 50 and 110 seconds. This final scenario is unlikely, however, because
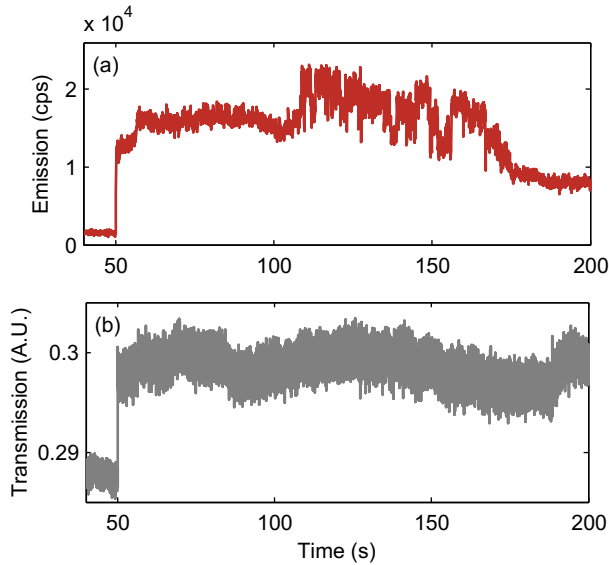
Figure 3.14: The (a) emission and (b) 1064 nm transmission channels show a stepwise increase in signal at 50 seconds, indicating individual scQD trapping.

trapping particles or clusters larger than the 38 nm gap is not expected. Large particles and clusters are prevented from peak trapping potentials at the bottom of the aperture[17]. In general, the trapping here was more of one-off event, since we were using a size distribution of particles and a distribution of different bowtie shapes. Further optimization is required in order to make trapping routine.

Emission dynamics for two more trapping experiments are shown in Figure 3.15, with emission and transmission channels for the 56 nm gap aperture in 3.15a and 3.15b, and emission and transmission channels for the 38 nm gap aperture in figure 3.15c and 3.15d. Both experiments used filtered scQDs (Fig. 3.6) with a mean hydrodynamic diameter of 21.1 nm. Successful trapping of particles smaller than the minimum size predicted by force calcula-

tions in both of these apertures can be rationalized by two possible explanations. Firstly, non-optical mechanisms described in the main text may contribute to trapping. Secondly, the trapped particle size could lie in the tail end of the size distribution as determined by DLS measurements (Fig. 3.6), which extends out to 45 nm in diameter for the filtered particles.

The first trapping experiment using the 56 nm aperture shows an increase in 1064 nm trapping laser transmission at 200 seconds (Fig. 3.15b), indicating particle trapping. The corresponding emission trace (Fig. 3.15a), however, does not exhibit emission until 260 seconds into the experiment, which is intermittent and resembles QD blinking. The second trapping experiment using the 38 nm aperture shows initial trapping in both the 1064 nm transmission (Fig. 3.15d) and the emission (Fig. 3.15c) at 210 seconds into the experiment. Subsequent trapping events, however, show subtle increases in 1064 nm transmission at 265 and 280 seconds, with corresponding emission events that rapidly decay in intensity after trapping. They all have similar increase both in fluorescence and transmission signal, most probably due to individual quantum dots trapped. We believe that it is unlikely that this situation could be due to three different aggregates.

Figure 3.16 shows spectra collected from the same aperture before and after scQD trapping and serves as evidence for two-photon excitation in the absence of a sub-bandgap excitation source. The spectral range between 520 nm to 700 nm is dark prior to trapping,
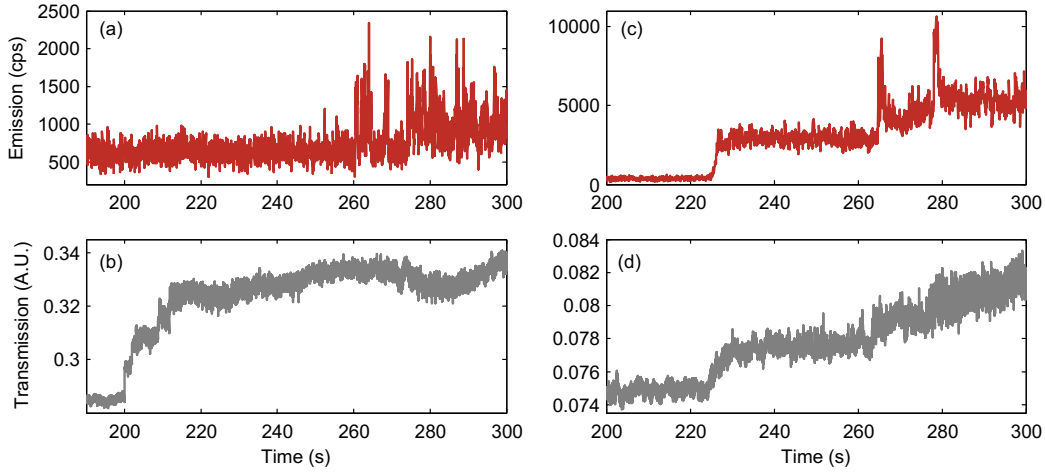
Figure 3.15: (a) Emission and (b) 1064 nm transmission for filtered scQDs in the 56 nm aperture shows evidence to QD blinking inside the optical trap. Multiple trapping events are detected in the (c) emission and (d) 1064 nm transmission channels for filtered scQDs in the 38 nm aperture that exhibit rapid quenching at 265 and 280 seconds in the emission channel only.

but a scQD emission peak appears at 640 nm after the particle is trapped. Additionally, the absence of detected signal at 532 nm rules out second harmonic generation in the aperture by the trapping beam. The emission and transmission intensities for this trapping event are given in the Fig. 3.17. Given the simulated peak intensity enhancement of $\sim 48\times$ for this aperture with a scQD in the aperture (Fig. 3.10a, the enhancement around the scQD not the corner), the enhanced excitation flux at the trapped scQD is calculated to be 74.9 MW/cm². This enhanced excitation flux, suitable for two-photon excitation of QDs[72], can be reached with a very low incident flux of 1.56 MW/cm² at 1064 nm, due to the strong plasmonic enhancement provided by the aperture[84]. We note that the enhanced flux inside the aperture is a factor of five larger than the flux reported using free space trapping[71].
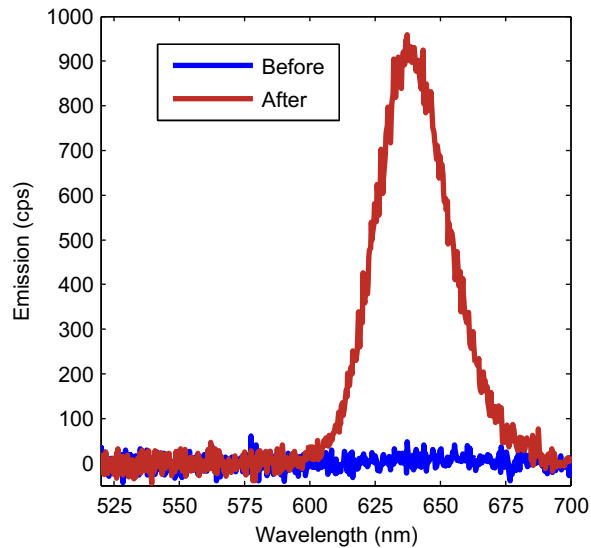
Figure 3.16: QD emission spectra before (blue) and after (red) optical trapping and two-photon excitation.

In Figure 3.17, the emission intensity was calculated by summing the spectral intensity of each frame from spectrometer/CCD camera detection scheme. Spectra were collected with 1 second integration times, resulting in poor time resolution in the emission channel. Trapping occurred at 279 seconds and was stable until the trial ended at 300 seconds.

3.9 Two-photon Photoluminescence of QDs on Silver Film

The most direct evidence to prove the QD inside the trap undergoes two-photon excitation is measuring the power dependence of the Two-photon Photoluminescence (TPPL). However, measuring TPPL with QD inside the aperture. The main reason was complication associated with varying the incident power over large range, while still having particles
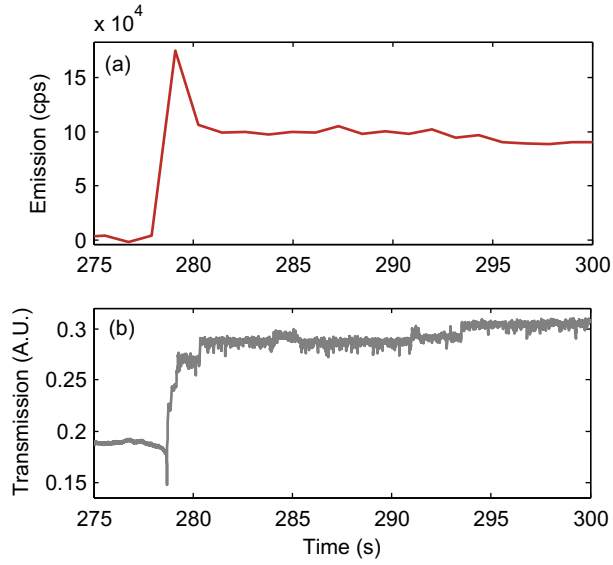
Figure 3.17: (a) Emission and (b) 1064 nm transmission channels for spectrally resolved emission detection presented in manuscript figure 3.16.

trapped. Therefore, we measured the power dependence when QDs were drop-coated on the same silver film. Due to local electric field enhancement, the QD still emitted fluorescence under the illumination of the 1064 nm trapping laser. The squared dependence of the input power shows that the excitation was indeed due to two-photon excitation (Fig. 3.18). Since the apertures feature much higher optical intensity than silver film, two-photon excitation becomes even more likely. Therefore, based on this indirect measurement, we conclude that our luminescent data is indeed due to TPPL.
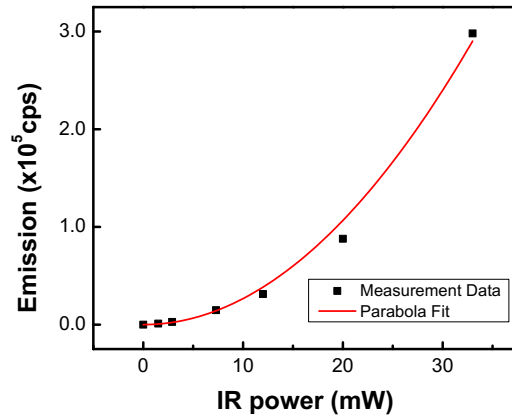
Figure 3.18: The fluorescence intensity versus input power, showing the squared dependence.

3.10 OUTLOOK AND CONCLUSION

The system presented here offers unique opportunities to study light-matter interactions

inside a plasmonic cavity[85]. In the experiments, scQDs did not stay inside the aperture af-

ter turning off the trapping laser, so the particle can be controllably placed and removed

from the aperture by toggling the trapping beam, allowing for convenient measurements

of the emitter inside and outside of the cavity. The optical trap also provides natural align-

ment of the nanoparticle to the peak field intensity in the aperture, alleviating concerns

over particle placement in a resonant cavity[86]. And the lift-off nature of the aperture fabri-

cation can enable fabrication of large arrays of apertures, each designed to operate at slightly

different wavelength, allowing for high throughput cavity resonance optimization. When

combined with our trapping based incorporation of QDs, this can eliminate the need for

57

post-fabrication cavity tuning and trimming: it is always possible to find and work with a resonator that is tuned to the emission wavelength of the emitter. Additionally, the platform might enable studies of individual QD absorption spectrum over wide wavelength range. This can be difficult using free-space approaches due to orders of magnitude difference between the absorption cross-section of the QD and the diffraction limited focal spot. This issue can be alleviated with our device due to the confined gap mode and the fact that aperture nature ensures that orders of more transmitted light interacts with QD trapped inside the aperture. Lastly, experiments need not be limited to scQDs. Emitter-cavity interactions can be investigated for alternative quantum emitters including nitrogen-vacancy centers in diamond[49], semiconductor nanorods, and hybrid structures[87].

In conclusion, bowtie apertures were designed and fabricated to optically trap 30 nm insulated QDs, yielding a system with stable single particle trapping and robust two-photon excitation at modest flux. Lift-off aperture fabrication was introduced and FDTD simulations revealed favorable trapping conditions that may be further aided by non-optical mechanisms. This system may enable the high-throughput experimentation of light-matter interactions and multiphoton processes in various types of emitters.

4

Coupling SiV Centers to Plasmonic

Nano-cavities

Beyond trapping, plasmonic cavities can also affect the emission properties of emitters placed inside. In this chapter, we describe an application of such cavities towards quantum network using photons, specifically those emitted from fluorescence defect centers in

diamond.

Defect centers in diamond are great candidates for quantum information processing due to their many advantages, such as high brightness, photostability, room temperature operation and presence of coherent spins which can be used as qubits. The defect center thus provides the main components of a quantum network: spins which can store information as quantum nodes, and single photons which exchange the information between nodes. Single photons are also central to quantum cryptography, which ensures completely secure communication.

Among the defect centers in diamond, the silicon-vacancy (SiV) center has gained significant attention due to its outstanding properties: strong zero-phonon line (ZPL) emission ($\sim$ 70%), robustness to fabrication processes, nearly lifetime limited optical linewidths, and lifetime-comparable spectral diffusions in nano-structures[8]. These features make SiV a great candidate for the quantum optics applications.

SiV centers can either be used as pure single photon sources for quantum cryptography[88], or as qubits for quantum entanglement[89]. The ability to extract the single photons is crucial for those applications and depends on two factors: out-coupling efficiency and photon generation efficiency. Hence, to harness the potential of defect centers, it is of great importance to engineer their properties through nano-devices.

Out-coupling is poor for bulk diamond (limited to 3 % due to total internal reflection,

$n_{diamond}$ = 2.4 at 737 nm), which serves as motivation to sculpt the diamond on the nano- or micron-scale in order to increase the coupling efficiency. Nanowires[90] and solid immersion lenses[91,92] have been previously fabricated in order to increase the efficiency roughly by one order of magnitude, and tapered waveguide to optical fiber[93] can have a collection efficiency as high as > 90 %.

Another approach to enhance the photon counts is to increase the photon generation efficiency by engineering the radiative decay rate through Purcell enhancement[94]. In this case the number of the generated photons is enhanced due to an increased surrounding photon density of states. Purcell enhancement can be achieved by coupling the emitter to a cavity, with the enhanced factor given by:

$$P_F = \frac{g^2}{\gamma \kappa} = \frac{3}{4\pi} \left(\frac{\lambda}{n}\right)^3 \frac{Q}{V} \tag{4.1}$$

g is the coupling rate between the emitter and cavity; κ is the cavity decay rate; γ is the emitter decoherence rate; Q and V are the quality factor and mode volume of the cavity, respectively. We can see that P_F is proportional to Q/V. Thus a cavity featuring high quality factor and small mode volume is desired in order to achieve a high Purcell factor.

Here we define our figure of merit (FOM) as the multiplication of Purcell factor and out-coupling efficiency. Purcell factor is the enhanced factor of generated photon counts when pumped in saturation, and collection efficiency is the ratio of the collected photons

to all the generated photons. FOM indicates the amount of single photons we can actually collect.

In this chapter, we propose to use plasmonic cavities to achieve both enhanced Purcell factors and collection efficiencies[46]. According to simulations done in FDTD (Lumerical), the designed circular apertures can have Purcell factors of 18 and collection efficiencies of 15 %, when taking into account the tapered sidewall that results from diamond etching. The FOM of circular apertures is 90 time higher than the FOM of bulk diamond, whose Purcell factor is 1 and collection efficiency is 3 %. The measurements show that the majority of SiV centers inside circular apertures have lifetimes near 1 ns, and can be as short as 0.2 ns, which represents a $\sim$ 9-fold reduction over the $\sim$ 1.8 ns value typical for SiVs in bulk diamond. Importantly, we found that some of the SiVs maintain narrow optical linewidths of 330 MHz, comparable to the transform-limited linewidth of 150 MHz, as well as small spectral diffusion of $\pm$ 100 MHz, even in plasmonic nanostructures, most likely because SiVs are less sensitive to surface states than other common defect centers (e.g., nitrogen-vacancy (NV) center[95]). The narrow linewidth and reduced spectral diffusion are critical for applying our devices in quantum information science and technology.

The SiV center consists of one silicon atom sitting between two missing carbon atoms in
the diamond lattice (Figure 4.1(a) top). The energy level diagram is shown in Figure 4.1(a),
consisting of ground (^2E_g) and excited states(^2E_u), separated by energy corresponded to 737
nm (the ZPL). The advantage of SiV compared to NV is that it has a strong ZPL which
constitutes $\sim$ 70% of its total emission (versus 4 % for NV[96]). Spin-orbit coupling further
splits the degenerate levels in the excited and ground states, forming a four level system with
the allowed transitions A, B, C, D indicated (Figure 4.1(a)). Figure 4.1(b) shows a SiV pho-
toluminescence excitation (PLE) spectrum excited on-resonance (collection: > 760 nm)
featuring the four distinct transitions.

As can be seen from its atomic structure, the SiV has D_{3d} symmetry[97]. Importantly, the
inversion symmetry leads to no permanent electric dipole, so that the SiV energy levels are
not affected by fluctuations in the electric field. This is the reason that SiV can have highly
reduced spectral diffusion compared to that of NV which has only C_{3v} symmetry featuring
no inversion symmetry. The linewidth and spectral diffusion are two important factors for
quantum optics applications. The linewidth should be as close as possible to the transform-
limited linewidth, and spectral diffusion should be as small as possible so that the emitter
can be used for realization of quantum networks. While the NV center is very promising
for such applications, it requires intricate surface treatment and annealing to maintain the

(a)

ES splitting
Δe: 250GHz

^2E_u
excited state

ZPL:
737nm

A B C D

^2E_g
ground state

GS splitting
Δg: 50GHz

(b)
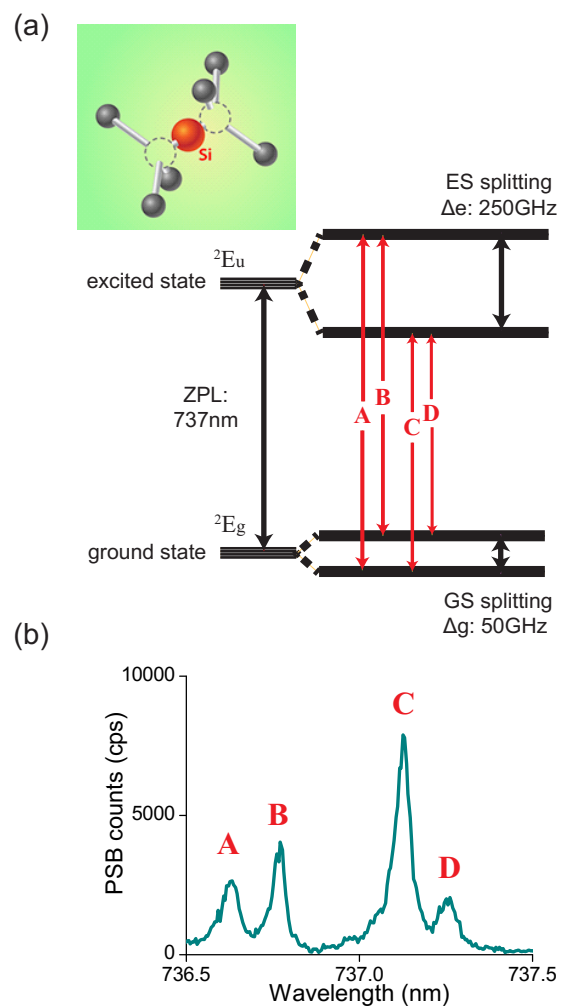
Figure 4.1: (a) Atomic structure (top) reproduced from the reference [7], and electronic structure (bottom) of the SiV. The excited and ground states have double spin and orbital degeneracy, and are split due to spin-orbit coupling. (b) Photoluminescence excitation of ensemble SiVs at $\sim$ 10 K. The four emission lines corresponding to the four transitions illustrated in (a) can clearly be seen.

transition stability[95]. However, SiV has the advantage of robustness to those surface states due to its symmetry as mentioned above. For example, recent work by the Lukin group at Harvard[8] showed that SiV centers implanted in 300 - 500 nm size waveguides have nearly transform-limited emission with minimal spectral diffusion and inhomogeneous broadening, both being smaller than the ZPL linewidth, which is critical for future applications such as quantum key distribution (Figure 4.2). Recently, it has been demonstrated that a single SiV inside a photonic crystal nanobeam can be a quantum optical switch[98]. This confirms that SiVs can be integrated in nano-photonics networks for future applications.

4.2 Introduction of plasmonic cavities

Plasmonic nano-resonators can strongly enhance the local field strength of the pump beam as well as the spontaneous decay rate of the SiV in order to improve single photon emission. As discussed in Chapter 2, although plasmonic cavities in general have low Q factors ($\sim 10 - 50$) due to the high losses in the metal, they can have extremely small mode volumes (10^{-2} to 10^{-3} $(\lambda/n)^3$). Thus it is still feasible to get moderately high Purcell factors through coupling quantum emitters to plasmonic cavities. In the past, Purcell factors larger than 1000 were achieved using silver nanowires or nanocubes on metal films with spacings of 5 to 15 nm[19,20]. Our group also successfully coupled NV centers to designed plasmonic cavities[99,49], showing both lifetime reduction and enhancement of saturation counts by a factor
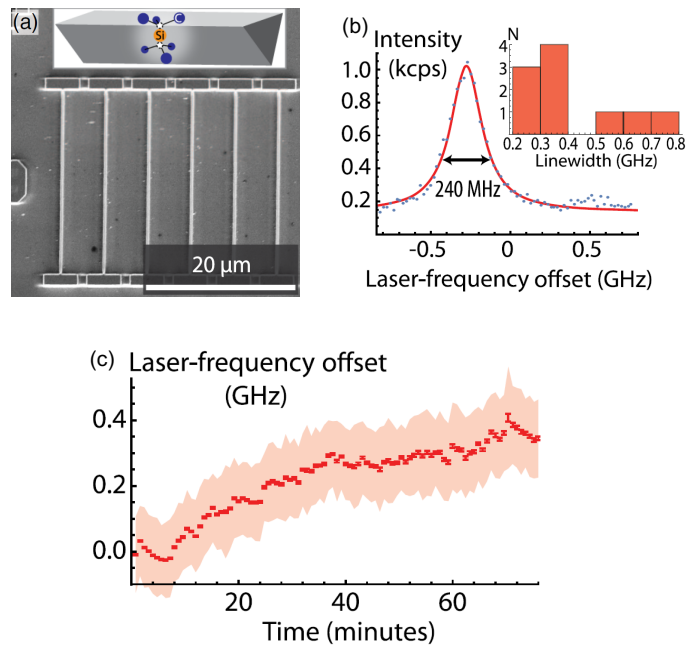
Figure 4.2: (a) SEM image of the nanobeam waveguides. Inset: schematic of a triangular diamond nanobeam containing an SiV center. (b) The linewidth of SiV inside nanobeam, showing the nearly transform limit property. Inset is the histogram of the SiV linewidths. (c) The transition shifted only by 400 MHz after one hour, proving the transition robustness of SiV. All the figures come from the reference [8].

of $\sim$ 7. We thus decided to use similar plasmonic nanocavities, but with higher collection efficiencies.

4.3 DESIGN

In this work, we proposed circular apertures to engineer the emission of SiV centers. An SEM image and schematic of our device are in Figure 4.3(a). By exciting the structure and collecting the emitted photons from the top, it is possible to increase the collection efficiency[46] compared to previous results where excitation and emission were on opposite sides of the diamond[99,49]. Simulations show that the Purcell enhancement for circular apertures with a diameter of 110 nm is $\sim$ 24, and a collection efficiency of $\sim$ 20%. The collection efficiency is obtained through calculating the far field pattern of the device and assuming the numerical aperture (NA) of collection objective is 0.9. From Figure 4.3(b), we can see that SiV emission mainly couples to the HE11 waveguide mode of the metallic circular aperture. This mode has a uniform field distribution over the cross section of the aperture, which makes the coupling easier. As can be seen from the side view of the mode's field profile, the supported resonance is a Fabry-Perot resonance with no node (FP-0 mode). Since it operates at the near zero-index mode, the resonance wavelength highly depends on the diameter of the aperture, but does not depend on the height of the pillars[46]. In other words, the additional physical length of the pillar does not contribute to its optical length since the mode
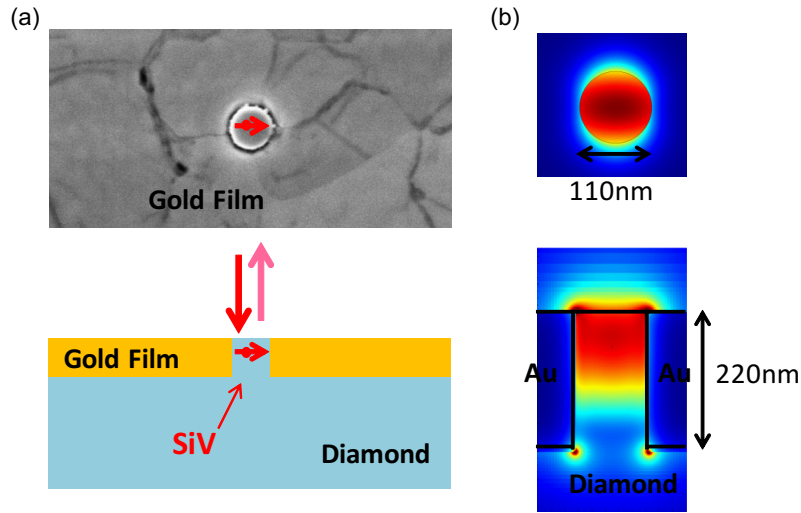
Figure 4.3: (a) Top: top view SEM image of the fabricated plasmonic aperture. Bottom: side view schematic of the device, showing the diamond pillar completely surrounded by gold film. (b) Field profile of the resonance. Top: HE11 mode of the aperture. Bottom: mode profile of side view showing it is FP-0 mode.

index is near zero.

However, due to the nature of etching, the sidewall of the pillar as produced during fabrication is always tapered (Figure 4.4(a), inset). The smallest slanted angle (ϑ in Figure 4.4) we could currently achieve is $\sim 6°$. This will slightly degrade the P_F and collection efficiency to $\sim$ 18 and $\sim$ 15%, respectively. Still, this $\sim$ 15 % collection efficiency is much higher than the one from previous single aperture devices (3 %)[99]. Another important difference between this and past work is that we chose gold as a metal layer. While gold is more lossy than silver, it is more robust and does not suffer from oxidation upon exposure to ambient conditions.
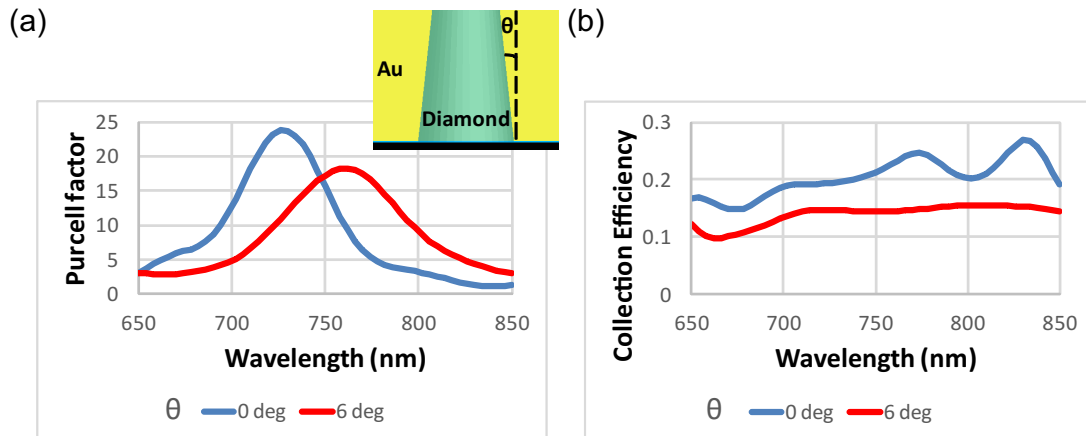
Figure 4.4: Simulations of the (a) Purcell factor and (b) collection efficiency for an aperture with slanted (red) or vertical (blue) sidewalls. We can see the 6°slanted wall degrade Purcell factor from 24 to 18, and collection efficiency from 20% to 15%.

4.4 Fabrication

The devices were fabricated in electronic grade diamond (Element Six). After mechanical polishing of the diamond surface, we did reactive-ion etching (RIE) to remove 1 μm of a resulting highly strained layer of diamond. Then, tri-acid cleaning (1:1:1, sulfuric:perchloric:nitric acids) was performed followed by Si implantation (Innovion Corp.). The implantation energy used was 75 keV, which corresponds to an implantation depth of 50 ± 10 nm according to SRIM (The Stopping and Range of Ions in Matter) simulations. After implantation, the diamond went through another round of tri-acid cleaning, followed by annealing in an alumina tube furnace in vacuum using a three step process to allow vacancy diffusion through the diamond lattice in order to form SiV centers: 400°C (8 hour annealing time), 800°C (12

69

hour annealing time), and 1100°C (2 hour annealing time)[100]. The tri-acid cleaning was performed again in order to remove the resulting graphitized surface. The yield of SiV centers is around 4% of the total implanted Si atoms.

Next, a thin Ti layer (15 nm) was deposited (e-beam evaporation, Denton) for better adhesion of the resist used for e-beam lithography. The diamond substrate was spin-coated with hydrogen silsesquioxane (HSQ), a negative tone electron-beam resist (FOX-16, Dow Corning). The resist was diluted with methyl isobutyl ketone (MIBK) in a 1:2 ratio of FOX:MIBK, in order to create a thinner resist that allows realization of smaller features. The circular patterns were created with e-beam lithography (Elionix ELS-F125) using dosages ranging from 3100 to 5000 $\mu C/cm^2$. The sample was developed in tetramethylammonium hydroxide (TMAH, 25% diluted solution) for 17 seconds, leaving behind 150 - 200 nm tall nano-posts. These were used as the mask during the RIE etching (Plasma-Therm) to create diamond pillars with embedded SiV centers. The first etch is 40 seconds of Ar/Cl_2 with 250 W RF biased power and 400 W ICP power, to remove the titanium layer. The second etch is 190 seconds under the condition of 60 mtorr O_2 with 100 W RF biased power and 700 W ICP power to create 220 nm tall nano-posts. Next, 220 nm thick gold was deposited followed by 650°C annealing for 7 minutes. The annealing results in gold reflow and reduces the gap between gold and diamond pillars, which is critical for good Purcell enhancement (Figure 4.6). Finally, sonication and lift-off in buffered oxide etch (BOE 5:1) were performed
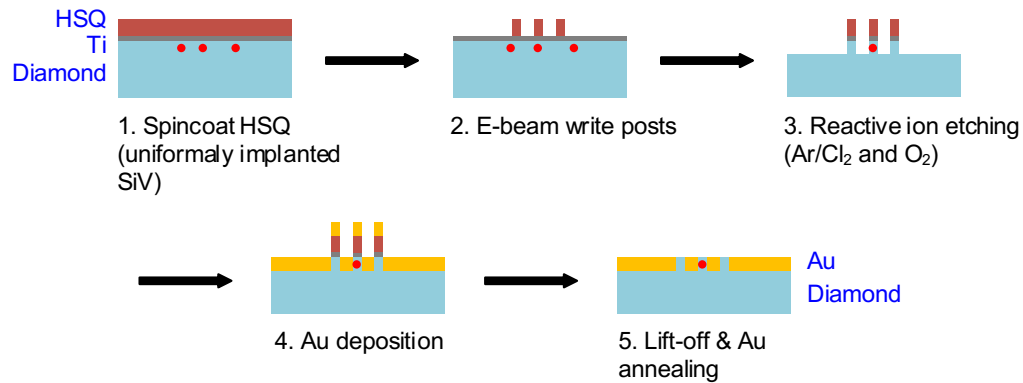
Figure 4.5: Schematic of the fabrication process used for our devices.

to get clean diamond gold apertures.

The gold annealing is critical for our device performance as it eliminates the gap between diamond and gold. Figure 4.6 shows that even a 5 nm gap results in a two-fold reduction of the Purcell effect, while a 15 nm gap results in a six-fold reduction. From the field profile on resonance, it can be seen that air gaps result in optical energy being concentrated in the gaps thus reducing its overlap with SiV and reducing the P_F.

4.5   SETUP

We used a home-built confocal microscope to characterize our plasmonic aperture devices. We first obtained a scanning image (Figure 4.7) by using off-resonant 700 nm excitation and collecting emission at the ZPL via a bandpass filter (740 nm with bandwidth 15 nm). We then measured the lifetimes, linewidths, and spectral diffusion characteristics of specific

(a)

Before annealing

~ **15nm**

After annealing @ 650⁰C

Gold Film

(b)
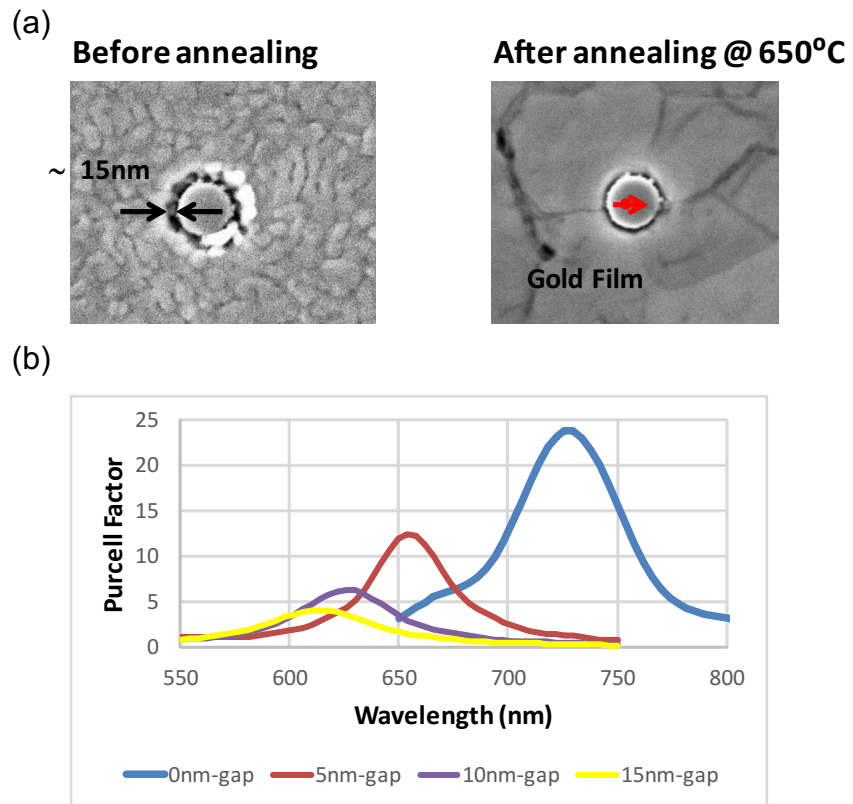
Figure 4.6: (a) The device before and after gold annealing, showing that annealing makes gold reflow and fill the gap. (b) Simulations of Purcell factors with different gap sizes. We can see that with a 15 nm gap, the Purcell factor already drops from 24 down to only 4.
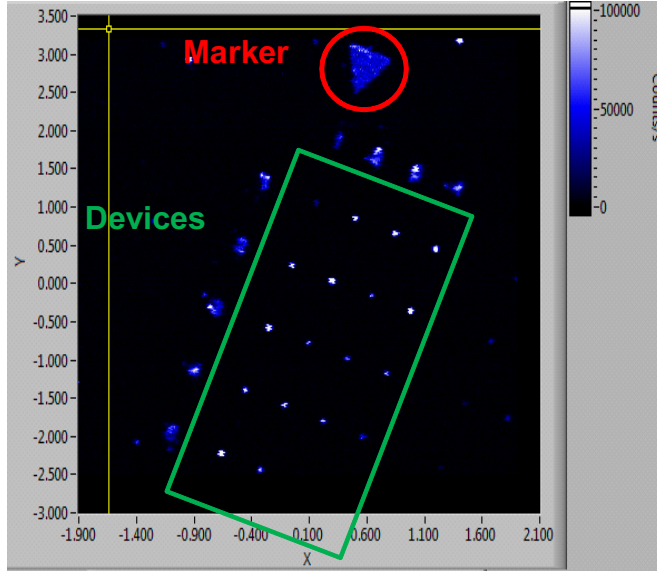
Figure 4.7: Confocal scanning image of the devices, off-resonance excitation.

SiVs using resonant excitation (737 nm) and collection of phonon-sideband (PSB) emission above 760 nm. The first property was measured using a pulsed laser with a $\sim 15 - 20\,GHz$ bandwidth (Mira 800 laser and monochromator), while the last two were obtained with CW excitation (M-squared laser).

The setup for pulsed laser is shown in Figure 4.8. The femto-second pulses from Mira were sent into monochromator with 1200 g/mm grating, which can be used to select the desired laser emission wavelength. A slit was set in order to reduce the pulse bandwidth to $\sim 15 - 20\,GHz$ (that is, the duration increases to ~ 25 ps.). Figure 4.9(a) shows the resonant scanning of SiV ensemble, taken at the position of the marker (indicated in Figure 4.7). The clear four lines from SiV ensemble indicates small inhomogeneity of SiVs in our
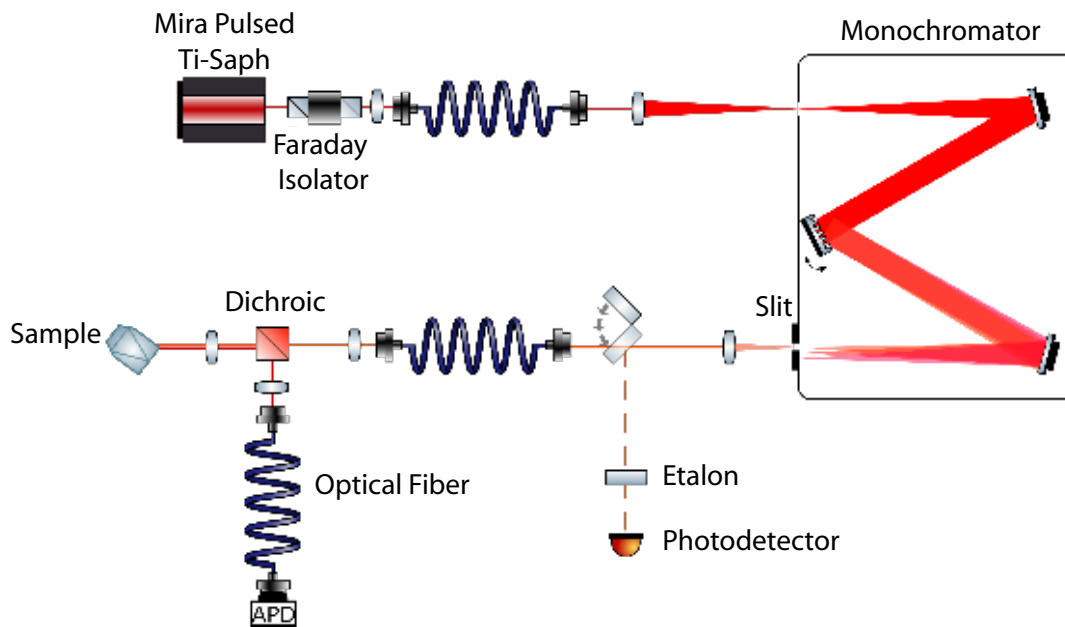
Figure 4.8: Schematic of the pulsed Ti:Sapphire laser and monochromator for resonant scanning of SiV. APD is avalanche photodiode.

samples.

4.6 LIFETIME MEASUREMENTS

We measured the lifetimes of the four lines in the ensemble SiVs, and they were found to be within 1.85 - 2 ns, consistent with previous literature (1.7 - 1.8 ns)[101,8]. Figure 4.9 shows a comparison of SiVs in the marker region versus plasmonic apertures. Interestingly, SiV transitions inside apertures span a relatively wide wavelength range ($\sim$ 7 nm) compared to that of bulk ($<$ 1 nm), which is likely caused by large local strain introduced by our fabrication process. We will describe this in a later section.
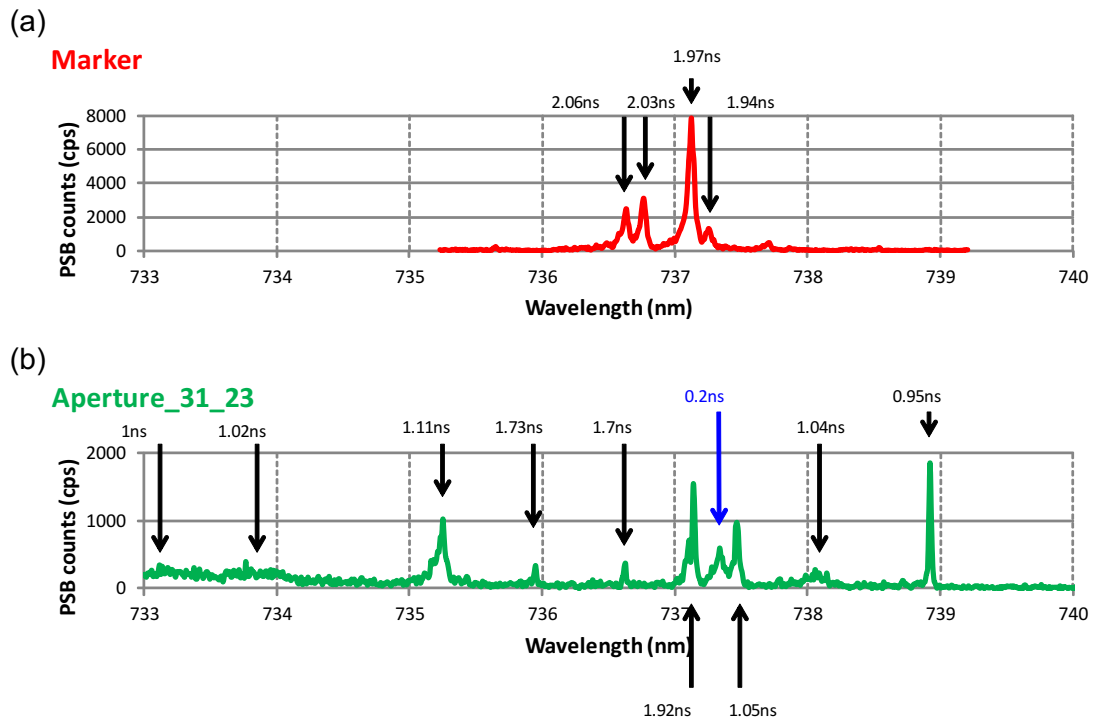
Figure 4.9: The PLE spectrum of the (a) ensemble SiVs in the marker and (b) few SiVs in the device. The transitions in the plasmonic devices are mostly single SiV (confirmed by CW pumping measurements shown later), and span a relatively wide wavelength range, indicative of large local strain fields. The lifetime of each transition was measured using pulsed excitation and is indicated in (b). An example of a transition with the remarkably low lifetime of 0.2 ns is indicated in blue.

(a) **With gold (plasmonic apertures)**

(b) **Without gold (nanopillars)**
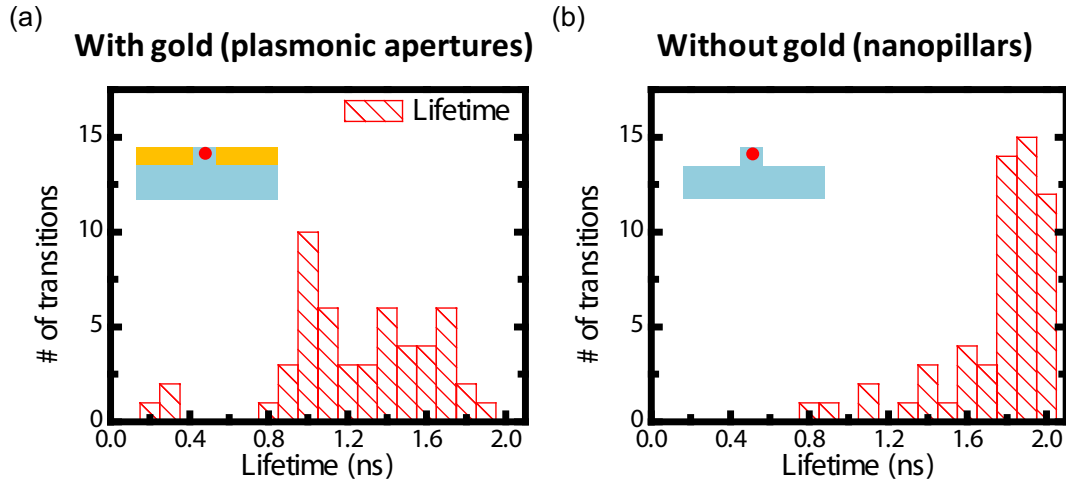
Figure 4.10: Histogram of the SiV lifetimes inside plasmonic nanocavities (a) before and (b) after removing gold, showing that the lifetime reduction is truly due to plasmonic cavities.

Resonant excitation enables us to address a specific SiV transition. By sending the PSB fluorescence and Ti:Sapphire laser signal into a time-correlated single photon counting system (TCSCPM, PicoHarp), we can measure the lifetime of individual SiV transitions. Due to the position and dipole polarization of the SiV inside the nano-cavity, different transitions have different lifetimes. Figure 4.10 shows a histogram of the lifetime measurements of our plasmonic devices. The measurements show that SiV centers inside circular apertures can have lifetimes as short as 0.2 ns, while most of them range from 0.9 to 1.7 ns. 0.2 ns lifetime represents a $\sim$ 9-fold reduction over the typical value in bulk diamond (Figure 4.11).

The measured lifetime reduction in fact includes both radiative and non-radiative relaxations, because the number of collected photons depends not purely on radiative emission,
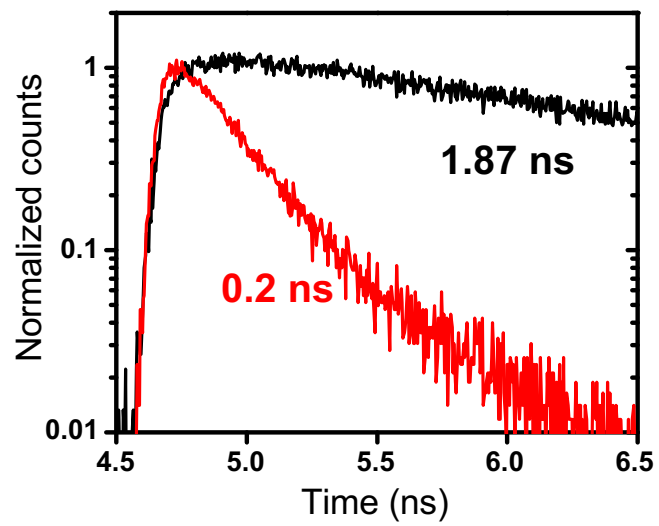
Figure 4.11: The lifetime comparison between the fastest SiV in our plasmonic apertures (red) and ensemble bulk SiVs (black). The shortest SiV lifetime in plasmonic apertures is ∼ 0.2 ns, which shows a ∼ 9-fold reduction over a typical ∼ 1.8 ns SiV lifetime.

but also on the availability of electrons in the excited state which can be reduced by non-radiative processes before a photon is emitted. The lifetime τ, is given by:

$$\frac{1}{\tau} = P_F \times \gamma_r + \gamma_{nr} \qquad (4.2)$$

where γ_r, γ_{nr} are radiative and non-radiative relaxation rate, respectively. The quantum efficiency (QE), which defines the relative amount of radiative emittions, is:

$$QE = \frac{\gamma_r}{\gamma_r + \gamma_{nr}} \qquad (4.3)$$

Given that the non-radiative relaxation might be large for SiV centers[98,102], the actual Purcell enhancement should be larger than the measured lifetime reduction. After removing gold, the lifetimes are mostly 1.6 to 2 ns, showing the lifetime reduction is truly due to our metal cavities. Here, the non-radiative relaxation is mainly due to relaxation through emitting phonons. The photon loss due to presence of absorbing metal layer is still regarded as radiative relaxation.

Here, we want to have a better estimation of the true Purcell enhancements. The exact QE of SiV centers is still under investigation, and believed to be a number between 0.1[98] and 0.3[102]. Assuming an intermediate value of QE $\sim$ 0.17, and selecting a 1 ns lifetime results in $P_F \sim 6$, which is in good agreement with what we observed for the similar de-

vices[99,103]. Since the HE11 resonance has quite uniform E-field distribution, statistically it is expected that most implanted SiVs will couple to this mode resulting in a lifetime of $\sim$ 1 ns. This is precisely what we observe in the histogram shown in Figure 4.10.

By assuming the same QE $\sim$ 0.17 and selecting the shortest measured lifetime of 0.2 ns, we obtain $P_F \sim$ 50. This experiment extracted value is larger than our simulated Purcell factors ($\sim$ 18), and can be explained if the SiV is close to metal. To verify this, we performed the simulations and found that when SiV is only 5 nm away from gold, the radiative enhancement can be as large as $\sim$ 50 (Figure 4.12). In these simulations we assumed a SiV polarization normal to the gold/diamond interface. This result is in agreement with previous work[104,19,20] where it was shown that a large enhancement in radiative rate is possible due to coupling to surface plasmon polariton (SPP) modes that feature large photon density of states. This comes at the expense of a reduction in photon extraction efficiency due to large losses of these plasmon modes. Indeed, in our devices, although the radiative enhancement is enlarged by 50, the collection efficiency drops down to only 4 %. In terms of FOM, the SiV which is 5 nm away from metal (200 %) is still inferior to the SiV in the center of the aperture (270 %).
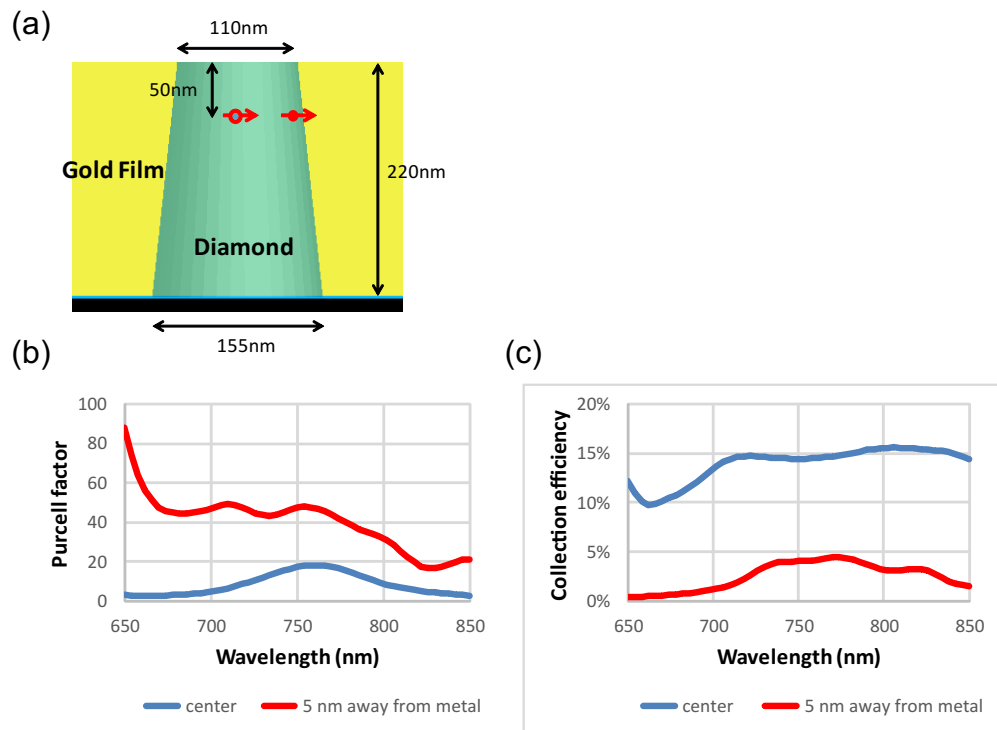
Figure 4.12: (a) Schematic of the device with two SiVs: one in the center and the other close to the metal. Simulations of (b) Purcell factor and (c) collection efficiency of two SiVs. We can see the one which is 5 nm away from the metal can have Purcell factor as high as ~ 50. However the collection efficiency drops down to only 4%.

4.7   Strain inside plasmonic apertures

As explained above, it is known that due to its inversion symmetry, the SiV does not have a permanent electric dipole, which means that spectral diffusion is highly reduced because the line cannot be shifted by a fluctuating electric field. However, SiV transitions possess a large strain susceptibility[105,100], significantly larger than for NV centers[106], for example. From Figure 4.9, we can see that the SiV transitions inside our plasmonic apertures experienced large shifts in their transition wavelengths from 737 nm, which were greatly suppressed upon removal of gold (Figure 4.13), strongly suggesting that strain is introduced by the gold film, possibly induced by gold annealing which creates a direct interface between gold and the diamond pillar. We measured many SiVs in multiple devices and have generated histograms of the transition wavelengths with and without gold (Figure 4.14). We can clearly see after removing gold, most of the transitions are "bunched" around the expected 737 nm wavelength.

To better understand the nature of the strain, we performed temperature studies of our devices. We increased the temperature from 11 K to 70 K in four steps and scanned the same SiV transition at each temperature. We observed that all the transitions (C lines in Figure 4.1) blue shift back to original 737 nm position at higher temperature, which is opposite to the normal red shift expected from temperature effect alone[107]. We also always found that the shift becomes larger for each temperature increment. The amount of shift differed for
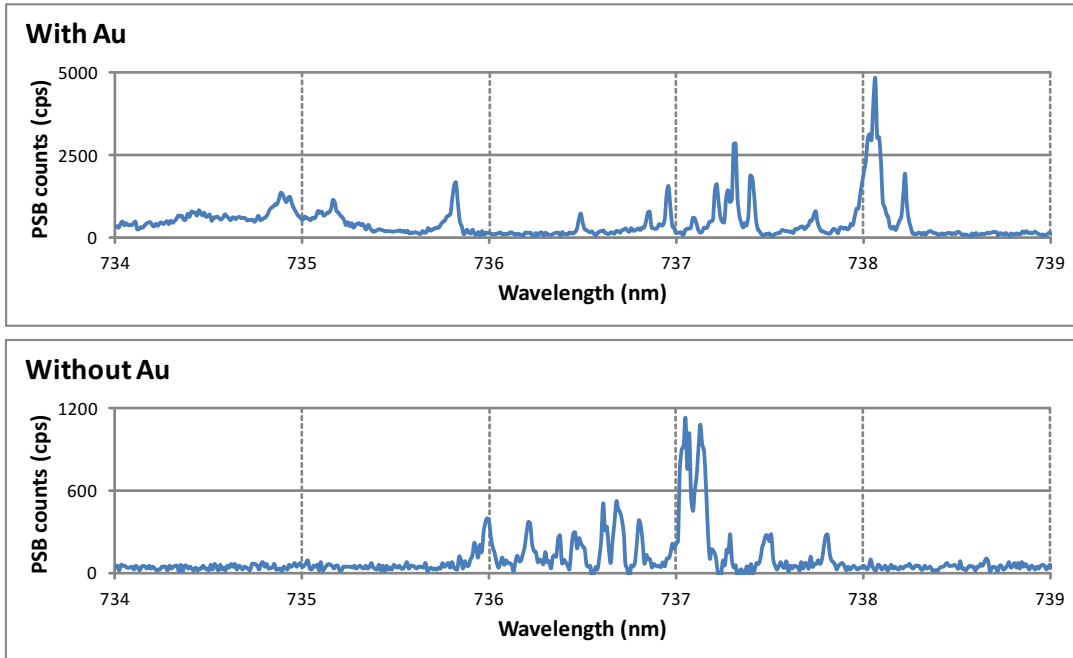
Figure 4.13: PLE spectrum of devices with and without gold. We can see without gold, most of the transitions are in the 737 nm range.
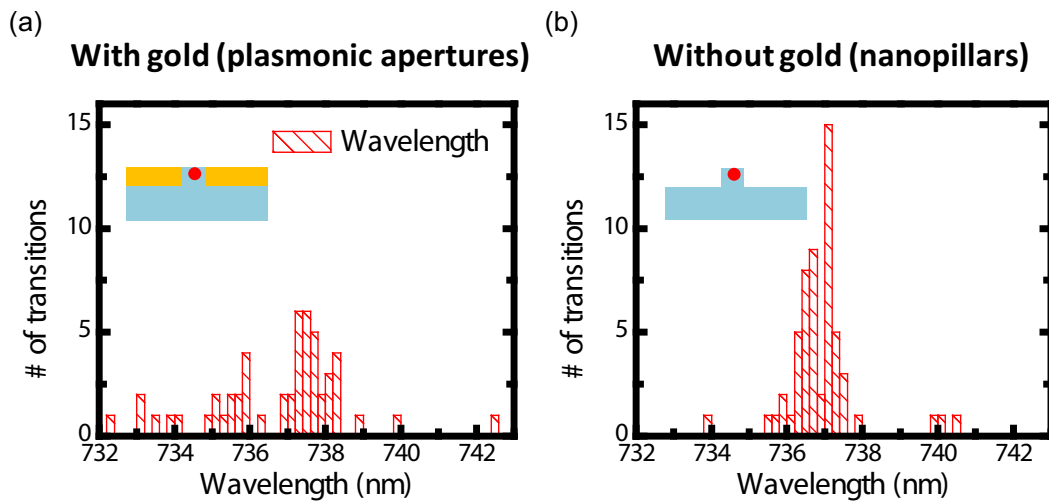
Figure 4.14: Histogram of the SiV line positions (a) before and (b) after removing gold. After removing gold away, the line position histogram is similar to ensemble fluorescence spectrum, further confirming that large spread in (b) is due to gold induced strain.

each transition, and we could not see any correlation between the amount of shift and line position. Based on temperature measurements we believe that different thermal expansion coefficients between Au and diamond result in different amount of induced strain which in turn results in different wavelength of transitions. The nature (tensile or compressive) of the large strain that we infer is not yet clear and is interesting to investigate further.

An interesting observation is that a transition features a particularly narrow linewidth when temperature increases, only ∼ 5 GHz at 70 K (Figure 4.15), which is 1 order of magnitude less than the other transitions. This is probably because the strain-induced splitting of the corresponded ground states is so large that the phonon density of states is greatly suppressed, and thus the dephasing in ground states is reduced. This is currently under investigation.

4.8 LINEWIDTH AND SPECTRAL DIFFUSION

As discussed, SiV has the advantage of robustness to surface states, and has stable transitions in nano-structures, such as 300 nm wide waveguides[8]. Here, we demonstrated that SiV can also be stable in our plasmonic apertures. Remarkably, even without post-annealing after our fabrication, we could still observe SiVs with narrow linewidths and little spectral diffusion (Figure 4.16). In order to further study the linewidth and spectral diffusion, the devices were cooled to 4 K and pumped with minimal laser power to avoid
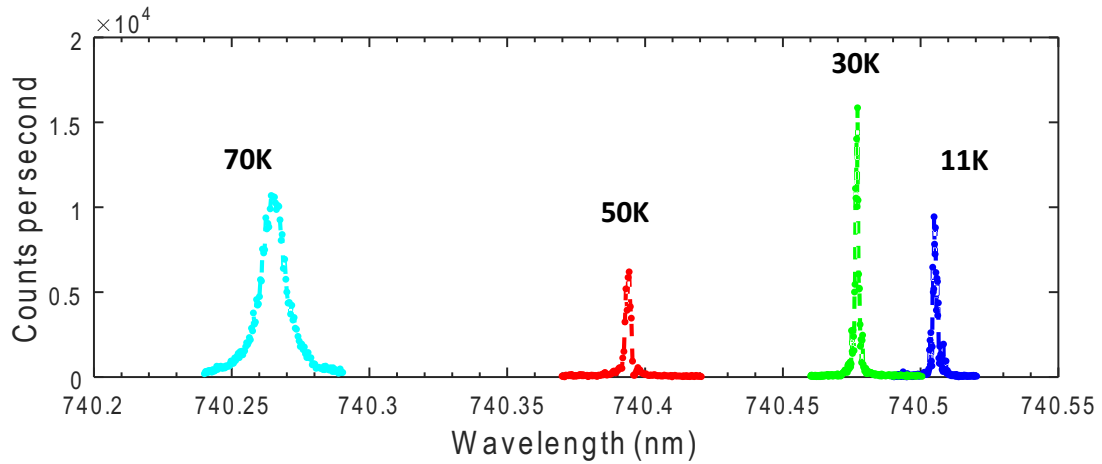
Figure 4.15: The same SiV PLE at different temperatures. It moves back to the normal 737 nm position as the temperature increases.

thermal contribution and power broadening. One of the measured SiV transitions has linewidth as narrow as 330 MHz (averaged over 45 scans to account for spectral diffusion which can be faster than the scanning speed, Figure 4.17), which is comparable to the transform limit of 150 MHz for the associated 1.1 ns lifetime. We attribute the difference to thermal broadening and spectral diffusion. Due to the field enhancement of plasmonic apertures, 10 nW is enough to see clear transitions.

Using our 45 scans (Figure 4.17), we could also measure the spectral diffusion of our device. The spectral diffusion is within the linewidth ($\pm$ 100 MHz), which is comparable to what has been observed in the case of SiVs in nanostructures[8]. Note that due to beam drifting, we could only do 10 consecutive scans, optimize the focus, and do another 10 con-

84
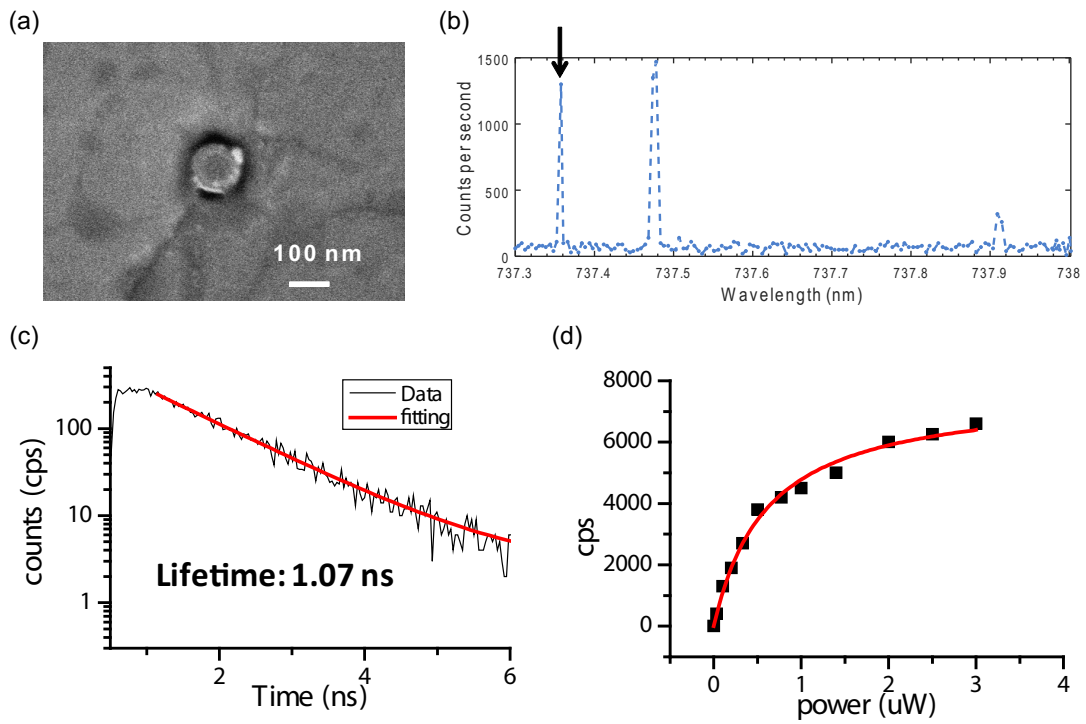
Figure 4.16: (a) SEM image of the plasmonic aperture device. (b) PLE spectrum of the device. The arrow points to the measured transition. (c) The lifetime of the transition is ~ 1.1 ns. (d) Saturation power measurements when pumped with CW laser on the transition. The counts are the PSB counts.
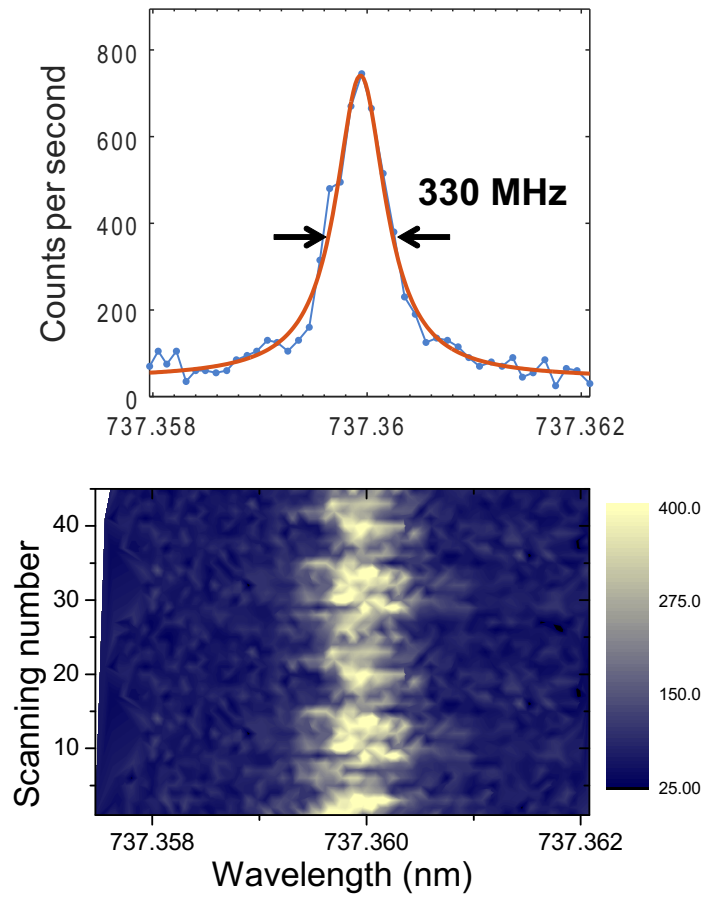
Figure 4.17: Linewidth and spectral diffusion of the SiV inside the plasmonic aperture. The temperature is 4 K and the excitation power is 10 nW. (a) The average linewidth is 330 MHz, which is comparable to the transform limit of 150 MHz. (b) The 45 scans over the same transition. This shows the transition is stable, and the spectral diffusion is within one linewidth ($\pm$ 100 MHz).

(a)

(b)

(c)
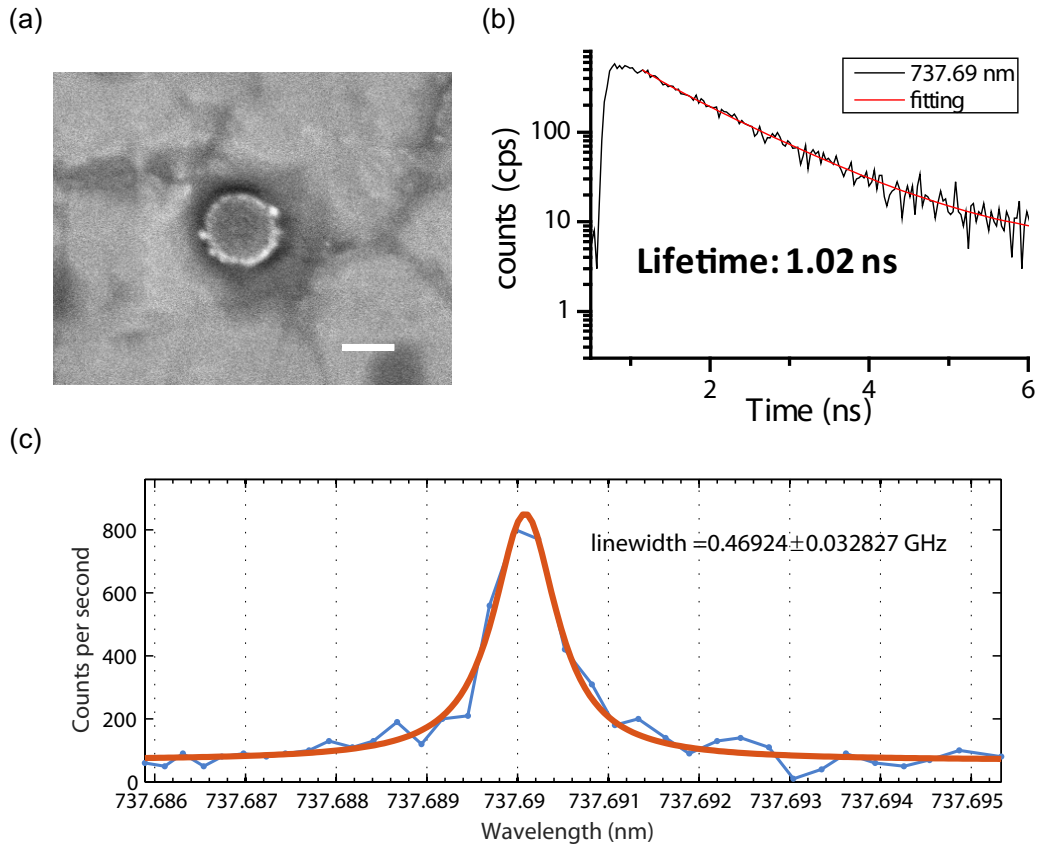
Figure 4.18: (a) The SEM image of the plasmonic aperture device. (b) The lifetime of the transition is $\sim$ 1 ns. (c) The linewidth is $\sim$ 470 MHz under the temperature of 10 K and the exciting power of 200 nW. The linewidth can be further reduced if lowering the temperature down to 4 K.

secutive scans again. We could find 1 to 2 stable SiVs out of 10 in our plasmonic apertures.

Figure 4.18 is another example of nearly transform-limited linewidth SiV. The demonstration of narrow linewidth and little spectral diffusion shows that our devices can have applications in quantum optics.

The reduced lifetime of SiVs in our plasmonic devices is an evidence of Purcell enhancement. Purcell enhancements can be further confirmed with additional measurements of enhanced saturation counts. This measurement is challenging in our case because our devices have more than one SiV per aperture, and the transitions shifted after removing the gold, which made it difficult to compare the same SiV saturation counts with and without Au. In the future, we will fabricate devices with single emitters to enable better comparison of saturation counts.

In addition, a large applied local strain induced in our device could further split the two ground states into a regime with much lower phonon density of states. As a result, the short spin coherence T2 time in the ground state could be improved by orders of magnitude, which is a main issue in applying SiVs as quantum registers. The spin coherence T2 time will be confirmed by optically detected magnetic resonance (ODMR)??.

Beyond circular apertures, we also designed the bowtie apertures since they have smaller mode volume and thus higher Purcell enhancements. The P_F can be as high as 90 for a 20 nm gap bowtie aperture, and systematic investigation of those are ongoing.

In conclusion, we fabricated the gold circular nanoresonators on diamond to achieve Purcell enhancement for SiV centers. The simulations showed that Purcell factors of $\sim$ 18 and collection efficiencies of $\sim$ 15% can be achieved in our devices. Measurements demon-

strated the maximum lifetime reduction of 9, while most of the life reduction is 1.8 compared to SiVs in bulk diamond. Given that SiV has a low internal quantum efficiency, the Purcell factor should be higher than the lifetime reduction. Besides, we observed SiVs can have nearly transform-limited linewidth and linewidth-comparable spectral diffusion. This shows that our devices can have applications for quantum networks.

References

[1] Stefan Alexander Maier. Plasmonics: fundamentals and applications. Springer Science & Business Media, 2007.

[2] Heinz Raether. Surface plasmons on smooth surfaces. Springer, 1988.

[3] P. B. Johnson and R. W. Christy. Optical constants of the noble metals. Phys. Rev. B, 6:4370–4379, Dec 1972.

[4] Edward D Palik. Handbook of optical constants of solids, volume 3. Academic press, 1998.

[5] S. A. Empedocles and M. G. Bawendi. Influence of spectral diffusion on the line shapes of single cdse nanocrystallite quantum dots. The Journal of Physical Chemistry B, 103(11):1826–1830, 1999.

[6] M. Nirmal, B. O Dabbousi, M. G Bawendi, J. J Macklin, J. K Trautman, T. D Harris, and L. E Brus. Fluorescence intermittency in single cadmium selenide nanocrystals. Nature, 383(6603):802–804, 1996.

[7] Guido Burkard. Diamond spins shining bright. Physics, 7:131, 2014.

[8] Ruffin E. Evans, Alp Sipahigil, Denis D. Sukachev, Alexander S. Zibrov, and Mikhail D. Lukin. Narrow-linewidth homogeneous optical emitters in diamond nanostructures via silicon ion implantation. Physical Review Applied, 5(4), 2016.

[9] Dmitri K. Gramotnev and Sergey I. Bozhevolnyi. Plasmonics beyond the diffraction limit. Nature Photonics, 4(2):83–91, 2010.

[10] J. A. Schuller, E. S. Barnard, W. Cai, Y. C. Jun, J. S. White, and M. L. Brongersma. Plasmonics for extreme light concentration and manipulation. Nat Mater, 9(3):193–204, 2010.

[11] D. K. Lim, K. S. Jeon, H. M. Kim, J. M. Nam, and Y. D. Suh. Nanogap-engineerable raman-active nanodumbbells for single-molecule detection. Nat Mater, 9(1):60–7, 2010.

[12] W. Zhu and K. B. Crozier. Quantum mechanical limit to plasmonic enhancement as observed by surface-enhanced raman scattering. Nat Commun, 5:5228, 2014.

[13] S. Kim, J. Jin, Y. J. Kim, I. Y. Park, Y. Kim, and S. W. Kim. High-harmonic generation by resonant plasmon field enhancement. Nature, 453(7196):757–60, 2008.

[14] P. Genevet, J. P. Tetienne, E. Gatzogiannis, R. Blanchard, M. A. Kats, M. O. Scully, and F. Capasso. Large enhancement of nonlinear optical phenomena by plasmonic nanocavity gratings. Nano Lett, 10(12):4880–3, 2010.

[15] Martti Kauranen and Anatoly V. Zayats. Nonlinear plasmonics. Nature Photonics, 6(11):737–748, 2012.

[16] Mathieu L. Juan, Reuven Gordon, Yuanjie Pang, Fatima Eftekhari, and Romain Quidant. Self-induced back-action optical trapping of dielectric nanoparticles. Nat Phys, 5(12):915–919, December 2009.

[17] Yuanjie Pang and Reuven Gordon. Optical trapping of 12 nm dielectric spheres using double-nanoholes in a gold film. Nano Letters, 11(9):3763–3767, August 2011.

[18] Anika Kinkhabwala, Zongfu Yu, Shanhui Fan, Yuri Avlasevich, Klaus Mullen, and MoernerW. E. Large single-molecule fluorescence enhancements produced by a bowtie nanoantenna. Nat Photon, 3(11):654–657, November 2009.

[19] Kasey J. Russell, Tsung-Li Liu, Shanying Cui, and Evelyn L. Hu. Large spontaneous emission enhancement in plasmonic nanocavities. Nature Photonics, 6(7):459–462, 2012.

[20] Gleb M. Akselrod, Christos Argyropoulos, Thang B. Hoang, Cristian Ciracì, Chao Fang, Jiani Huang, David R. Smith, and Maiken H. Mikkelsen. Probing the mecha-

nisms of large purcell enhancement in plasmonic nanoantennas. Nature Photonics, 8(11):835–840, 2014.

[21] A. A. Saleh and J. A. Dionne. Toward efficient optical trapping of sub-10-nm particles with coaxial plasmonic apertures. Nano Lett, 12(11):5581–6, 2012.

[22] H. Im, K. C. Bantz, N. C. Lindquist, C. L. Haynes, and S. H. Oh. Vertically oriented sub-10-nm plasmonic nanogap arrays. Nano Lett, 10(6):2231–6, 2010.

[23] J. Theiss, P. Pavaskar, P. M. Echternach, R. E. Muller, and S. B. Cronin. Plasmonic nanoparticle arrays with nanometer separation for high-performance sers substrates. Nano Lett, 10(8):2749–54, 2010.

[24] Jonathan A. Fan, Chihhui Wu, Kui Bao, Jiming Bao, Rizia Bardhan, Naomi J. Halas, Vinothan N. Manoharan, Peter Nordlander, Gennady Shvets, and Federico Capasso. Self-assembled plasmonic nanoparticle clusters. Science, 328(5982):1135–1138, 2010.

[25] W. Zhu, M. G. Banaee, D. Wang, Y. Chu, and K. B. Crozier. Lithographically fabricated optical antennas with gaps well below 10 nm. Small, 7(13):1761–6, 2011.

[26] A. Zehtabi-Oskuie, A. A. Zinck, R. M. Gelfand, and R. Gordon. Template stripped double nanohole in a gold film for nano-optical tweezers. Nanotechnology, 25(49):495301, 2014.

[27] X. Chen, C. Ciraci, D. R. Smith, and S. H. Oh. Nanogap-enhanced infrared spectroscopy with template-stripped wafer-scale arrays of buried plasmonic cavities. Nano Lett, 15(1):107–13, 2015.

[28] J. Berthelot, S. S. Acimovic, M. L. Juan, M. P. Kreuzer, J. Renger, and R. Quidant. Three-dimensional manipulation with scanning near-field optical nanotweezers. Nat Nano, 9(4):295–299, April 2014.

[29] Russell A. Jensen, I. Chun Huang, Ou Chen, Jennifer T. Choy, Thomas S. Bischof, Marko Lončar, and Moungi G. Bawendi. Optical trapping and two-photon excitation of colloidal quantum dots using bowtie apertures. ACS Photonics, 2016.

[30] Xiaolei Wen, Luis M. Traverso, Pornsak Srisungsitthisunti, Xianfan Xu, and Euclid E. Moon. Optical nanolithography with $\lambda/15$ resolution using bowtie aperture array. Applied Physics A, 2014.

[31] Guowei Lu, Wenqiang Li, Tianyue Zhang, Song Yue, Jie Liu, Lei Hou, Zhi Li, and Qihuang Gong. Plasmonic-enhanced molecular fluorescence within isolated bowtie nano-apertures. ACS Nano, 6(2):1438–1448, 2012.

[32] M. Melli, A. Polyakov, D. Gargas, C. Huynh, L. Scipioni, W. Bao, D. F. Ogletree, P. J. Schuck, S. Cabrini, and A. Weber-Bargioni. Reaching the theoretical resonance

quality factor limit in coaxial plasmonic nanoresonators fabricated by helium ion lithography. Nano Lett, 13(6):2687–91, 2013.

[33] Liang Wang, Sreemanth M. Uppuluri, Eric X. Jin, and Xianfan Xu. Nanolithography using high transmission nanoscale bowtie apertures. Nano Letters, 6(3):361–364, 2006.

[34] O. Scholder, K. Jefimovs, I. Shorubalko, C. Hafner, U. Sennhauser, and G. L. Bona. Helium focused ion beam fabricated plasmonic antennas with sub-5 nm gaps. Nanotechnology, 24(39):395301, 2013.

[35] Y. Wang, M. Abb, S. A. Boden, J. Aizpurua, C. H. de Groot, and O. L. Muskens. Ultrafast nonlinear control of progressively loaded, single plasmonic nanoantennas fabricated using helium ion milling. Nano Lett, 13(11):5647–53, 2013.

[36] H. Kollmann, X. Piao, M. Esmann, S. F. Becker, D. Hou, C. Huynh, L. O. Kautschor, G. Bosker, H. Vieker, A. Beyer, A. Golzhauser, N. Park, R. Vogelgesang, M. Silies, and C. Lienau. Toward plasmonics with nanometer precision: nonlinear optics of helium-ion milled gold nanoantennas. Nano Lett, 14(8):4778–84, 2014.

[37] Kenji Yamazaki and Hideo Namatsu. 5-nm-order electron-beam lithography for nanodevice fabrication. Japanese Journal of Applied Physics, 43(6B):3767–3771, 2004.

[38] Joel K. W. Yang and Karl K. Berggren. Using high-contrast salty development of hydrogen silsesquioxane for sub-10-nm half-pitch lithography. Journal of Vacuum Science & Technology B: Microelectronics and Nanometer Structures, 25(6):2025, 2007.

[39] V. R. Manfrinato, L. Zhang, D. Su, H. Duan, R. G. Hobbs, E. A. Stach, and K. K. Berggren. Resolution limits of electron-beam lithography toward the atomic scale. Nano Lett, 13(4):1555–8, 2013.

[40] Huigao Duan, Hailong Hu, Karthik Kumar, Zexiang Shen, and Joel K. W. Yang. Direct and reliable patterning of plasmonic nanostructures with sub-10-nm gaps. ACS Nano, 5(9):7593–7600, 2011.

[41] Ai Leen Koh, David W. McComb, Stefan A. Maier, H. Y. Low, and Joel K. W. Yang. Sub-10 nm patterning of gold nanostructures on silicon-nitride membranes for plasmon mapping with electron energy-loss spectroscopy. Journal of Vacuum Science & Technology B: Microelectronics and Nanometer Structures, 28(6):C6O45, 2010.

[42] H. Duan, A. I. Fernandez-Dominguez, M. Bosman, S. A. Maier, and J. K. Yang. Nanoplasmonics: classical down to the nanometer scale. Nano Lett, 12(3):1683–9, 2012.

[43] Hongcang Guo, Todd P. Meyrath, Thomas Zentgraf, Na Liu, Liwei Fu, Heinz Schweizer, and Harald Giessen. Optical resonances of bowtie slot antennas and their geometry and material dependence. Optics Express, 16(11):7756–7766, 2008.

[44] I. A. Ibrahim, M. Mivelle, T. Grosjean, J. T. Allegre, G. W. Burr, and F. I. Baida. Bowtie-shaped nanoaperture: a modal study. Optics Letters, 35(14):2448–2450, 2010.

[45] I-Chun Huang, Jeffrey Holzgrafe, Russell A. Jensen, Jennifer T. Choy, Moungi G. Bawendi, and Marko Lončar. 10 nm gap bowtie plasmonic apertures fabricated by modified lift-off process. Applied Physics Letters, 109(13):133105, 2016.

[46] Irfan Bulu, Thomas Babinec, Birgit Hausmann, Jennifer T. Choy, and Marko Lon-car. Plasmonic resonators for enhanced diamond NV- center single photon sources. Optics Express, 19(6):5268–5276, 2011.

[47] B. Prade and J. Y. Vinet. Guided optical waves in fibers with negative dielectric constant. Lightwave Technology, Journal of, 12(1):6–18, 1994.

[48] Feng Wang and Y. Ron Shen. General properties of local plasmons in metal nanostructures. Physical Review Letters, 97(20), 2006.

[49] Jennifer T. Choy, Irfan Bulu, Birgit J. M. Hausmann, Erika Janitz, I-Chun Huang, and Marko Lončar. Spontaneous emission and collection efficiency enhancement

of single emitters in diamond via plasmonic cavities and gratings. Applied Physics Letters, 103(16):161101, 2013.

[50] A. V. Akimov, A. Mukherjee, C. L. Yu, D. E. Chang, A. S. Zibrov, P. R. Hemmer, H. Park, and M. D. Lukin. Generation of single optical plasmons in metallic nanowires coupled to quantum dots. Nature, 450(7168):402–6, 2007.

[51] K. Kumar, H. Duan, R. S. Hegde, S. C. Koh, J. N. Wei, and J. K. Yang. Printing colour at the optical diffraction limit. Nat Nanotechnol, 7(9):557–61, 2012.

[52] Julien Houel, Sébastien Sauvage, Philippe Boucaud, Alexandre Dazzi, Rui Prazeres, Fran çois Glotin, Jean-Michel Ortéga, Audrey Miard, and Aristide Lemaître. Ultraweak-absorption microscopy of a single semiconductor quantum dot in the midinfrared range. Phys. Rev. Lett., 99:217404, Nov 2007.

[53] Alexandre Aubry, Dang Yuan Lei, Stefan A. Maier, and J. B. Pendry. Broadband plasmonic device concentrating the energy at the nanoscale: The crescent-shaped cylinder. Phys. Rev. B, 82:125430, Sep 2010.

[54] Pornsak Srisungsitthisunti, Okan K. Ersoy, and Xianfan Xu. Improving near-field confinement of a bowtie aperture using surface plasmon polaritons. Applied Physics Letters, 98(22):223106, 2011.

[55] A. Ashkin, J. M. Dziedzic, J. E. Bjorkholm, and Steven Chu. Observation of a single-beam gradient force optical trap for dielectric particles. Optics Letters, 11(5):288–290, 1986.

[56] Maurizio Righini, Anna S. Zelenina, Christian Girard, and Romain Quidant. Parallel and selective trapping in a patterned plasmonic landscape. Nature Physics, 3(7):477–480, 2007.

[57] A. N. Grigorenko, N. W. Roberts, M. R. Dickinson, and Y. Zhang. Nanometric optical tweezers based on nanostructured substrates. Nature Photonics, 2(6):365–370, 2008.

[58] M. Righini, P. Ghenuche, S. Cherukulappurath, V. Myroshnychenko, F. J. García de Abajo, and R. Quidant. Nano-optical trapping of rayleigh particles and escherichia coli bacteria with resonant optical antennas. Nano Letters, 9(10):3387–3391, 2009.

[59] Mathieu L Juan, Maurizio Righini, and Romain Quidant. Plasmon nano-optical tweezers. Nat Photon, 5(6):349–356, June 2011.

[60] K. Wang, E. Schonbrun, P. Steinvurzel, and K. B. Crozier. Trapping and rotating nanoparticles using a plasmonic nano-tweezer with an integrated heat sink. Nat Commun, 2:469, 2011.

[61] Y. Tanaka, S. Kaneda, and K. Sasaki. Nanostructured potential of optical trapping using a plasmonic nanoblock pair. Nano Lett, 13(5):2146–50, 2013.

[62] Chang Chen, Mathieu L. Juan, Yi Li, Guido Maes, Gustaaf Borghs, Pol Van Dorpe, and Romain Quidant. Enhanced optical trapping and arrangement of nano-objects in a plasmonic nanocavity. Nano Letters, 12(1):125–132, December 2011.

[63] L. Novotny and B. Hecht. Principles of Nano-Optics. Cambridge University Press, 2006.

[64] M. Mivelle, T. S. van Zanten, L. Neumann, N. F. van Hulst, and M. F. Garcia-Parajo. Ultrabright bowtie nanoaperture antenna probes studied by single molecule fluorescence. Nano Lett, 12(11):5972–8, 2012.

[65] Poul Martin Hansen, Vikram Kjøller Bhatia, Niels Harrit, and Lene Oddershede. Expanding the optical trapping range of gold nanoparticles. Nano Letters, 5(10):1937–1942, 2005.

[66] Peter J. Pauzauskie, Aleksandra Radenovic, Eliane Trepagnier, Hari Shroff, Peidong Yang, and Jan Liphardt. Optical trapping and integration of semiconductor nanowire assemblies in water. Nat Mater, 5(2):97–101, February 2006.

[67] Christine Selhuber-Unkel, Inga Zins, Olaf Schubert, Carsten Sönnichsen, and Lene B. Oddershede. Quantitative optical trapping of single gold nanorods. Nano Letters, 8(9):2998–3003, 2008.

[68] C. Robin Head, Elena Kammann, Marco Zanella, Liberato Manna, and Pavlos G. Lagoudakis. Spinning nanorods - active optical manipulation of semiconductor nanorods using polarised light. Nanoscale, 4:3693–3697, 2012.

[69] Yuanjie Pang and Reuven Gordon. Optical trapping of a single protein. Nano Letters, 12(1):402–406, 2012.

[70] A. Ashkin, J. M. Dziedzic, and T. Yamane. Optical trapping and manipulation of single cells using infrared laser beams. Nature, 330(6150):769–771, December 1987.

[71] Liselotte Jauffred, Andrew C. Richardson, and Lene B. Oddershede. Three-dimensional optical control of individual quantum dots. Nano Letters, 8(10):3376–3380, 2008.

[72] Liselotte Jauffred and Lene B. Oddershede. Two-photon quantum dot excitation during optical trapping. Nano Letters, 10(5):1927–1930, 2010.

[73] The idex of refraction is 2.5367 at 1064 nm for bulk CdSe.

[74] Sean A. Blanton, Ahmad Dehestani, Peter C. Lin, and Philippe Guyot-Sionnest. Photoluminescence of single semiconductor nanocrystallites by two-photon excitation microscopy. Chemical Physics Letters, 229(3):317 – 322, 1994.

[75] Daniel R. Larson, Warren R. Zipfel, Rebecca M. Williams, Stephen W. Clark, Marcel P. Bruchez, Frank W. Wise, and Watt W. Webb. Water-soluble quantum dots for multiphoton fluorescence imaging in vivo. Science, 300(5624):1434–1436, 2003.

[76] Wei-Yi Chiang, Tomoki Okuhata, Anwar Usman, Naoto Tamai, and Hiroshi Masuhara. Efficient optical trapping of CdTe quantum dots by femtosecond laser pulses. The Journal of Physical Chemistry B, ASAP(0):0, June 2014.

[77] Yasuyuki Tsuboi, Tatsuya Shoji, Noboru Kitamura, Mai Takase, Kei Murakoshi, Yoshihiko Mizumoto, and Hajime Ishihara. Optical trapping of quantum dots based on gap-mode-excitation of localized surface plasmon. The Journal of Physical Chemistry Letters, 1(15):2327–2333, 2010.

[78] Ana Zehtabi-Oskuie, Hao Jiang, Bryce R. Cyr, Douglas W. Rennehan, Ahmed A. Al-Balushi, and Reuven Gordon. Double nanohole optical trapping: dynamics and protein-antibody co-trapping. Lab Chip, 13(13):2563–2568, 2013.

[79] Ou Chen, Jing Zhao, Vikash P. Chauhan, Jian Cui, Cliff Wong, Daniel K. Harris, He Wei, Hee-Sun Han, Dai Fukumura, Rakesh K. Jain, and Moungi G. Bawendi.

Compact high-quality CdSe–CdS core–shell nanocrystals with narrow emission linewidths and suppressed blinking. Nat Mater, 12(5):445–451, May 2013.

[80] Ou Chen, Xian Chen, Yongan Yang, Jared Lynch, Huimeng Wu, Jiaqi Zhuang, and Y. Charles Cao. Synthesis of metal–selenide nanocrystals using selenium dioxide as the selenium precursor. Angewandte Chemie International Edition, 47(45):8638–8641, 2008.

[81] C Dineen, M Reichelt, S W Koch, and J V Moloney. Optical trapping of quantum dots in a metallic nanotrap. Journal of Optics A: Pure and Applied Optics, 11(11):114004, 2009.

[82] Abhay Kotnala and Reuven Gordon. Quantification of high-efficiency trapping of nanoparticles in a double nanohole optical tweezer. Nano Letters, 14(2):853–856, 2014.

[83] Liselotte Jauffred, Anders Kyrsting, Eva C. Arnspang, S. Nader S. Reihani, and Lene B. Oddershede. Sub-diffraction positioning of a two-photon excited and optically trapped quantum dot. Nanoscale, 6:6997–7003, 2014.

[84] Wim Wenseleers, Francesco Stellacci, Timo Meyer-Friedrichsen, Timo Mangel, Christina A. Bauer, Stephanie J. K. Pond, Seth R. Marder, and Joseph W. Perry. Five orders-of-magnitude enhancement of two-photon absorption for dyes on silver

nanoparticle fractal clusters. The Journal of Physical Chemistry B, 106(27):6853–6863, 2002.

[85] J. N. Farahani, D. W. Pohl, H.-J. Eisler, and B. Hecht. Single quantum dot coupled to a scanning optical antenna: A tunable superemitter. Phys. Rev. Lett., 95:017402, Jun 2005.

[86] M. Geiselmann, R. Marty, J. Renger, F. J. Garcia de Abajo, and R. Quidant. Deterministic optical-near-field-assisted positioning of nitrogen-vacancy centers. Nano Lett, 14(3):1520–5, 2014.

[87] Ou Chen, Lars Riedemann, Fred Etoc, Hendrik Herrmann, Mathieu Coppey, Mariya Barch, Christian T. Farrar, Jing Zhao, Oliver T. Bruns, He Wei, Peng Guo, Jian Cui, Russ Jensen, Yue Chen, Daniel K. Harris, Jose M. Cordero, Zhongwu Wang, Alan Jasanoff, Dai Fukumura, Rudolph Reimer, Maxime Dahan, Rakesh K. Jain, and Moungi G. Bawendi. Magneto-fluorescent core-shell supernanoparticles. Nature Communications, 5:5093, October 2014.

[88] Alexios Beveratos, Rosa Brouri, Thierry Gacoin, André Villing, Jean-Philippe Poizat, and Philippe Grangier. Single photon quantum cryptography. Phys. Rev. Lett., 89:187901, Oct 2002.

[89] H. Bernien, B. Hensen, W. Pfaff, G. Koolstra, M. S. Blok, L. Robledo, T. H. Taminiau, M. Markham, D. J. Twitchen, L. Childress, and R. Hanson. Heralded entanglement between solid-state qubits separated by three metres. Nature, 497(7447):86–90, 2013.

[90] Thomas M Babinec, Birgit JM Hausmann, Mughees Khan, Yinan Zhang, Jeronimo R Maze, Philip R Hemmer, and Marko Lončar. A diamond nanowire single-photon source. Nature nanotechnology, 5(3):195–199, 2010.

[91] P Siyushev, F Kaiser, V Jacques, I Gerhardt, S Bischof, H Fedder, J Dodson, M Markham, D Twitchen, F Jelezko, et al. Monolithic diamond optics for single photon detection. Applied physics letters, 97(24):241902, 2010.

[92] Tim Schröder, Friedemann Gädeke, Moritz Julian Banholzer, and Oliver Benson. Ultrabright and efficient single-photon generation based on nitrogen-vacancy centres in nanodiamonds on a solid immersion lens. New Journal of Physics, 13(5):055017, 2011.

[93] Michael J. Burek, Charles Meuwly, Ruffin E. Evans, Mihir K. Bhaskar, Alp Sipahigil, Srujan Meesala, Denis D. Sukachev, Christian T. Nguyen, Jose L. Pacheco, Edward Bielejec, Mikhail D. Lukin, and Marko Lončar. A fiber-coupled diamond quantum nanophotonic interface. arXiv: 1612.05285, Submitted.

[94] E. M. Purcell. Spontaneous emission probabilities at radio frequencies. volume 69, pages 681+, 1946.

[95] Y. Chu, N.P. de Leon, B.J. Shields, B. Hausmann, R. Evans, E. Togan, M. J. Burek, M. Markham, A. Stacey, A.S. Zibrov, A. Yacoby, D.J. Twitchen, M. Loncar, H. Park, P. Maletinsky, and M.D. Lukin. Coherent optical transitions in implanted nitrogen vacancy centers. Nano Letters, 14(4):1982–1986, 2014. PMID: 24588353.

[96] Igor Aharonovich and Elke Neu. Diamond nanophotonics. Advanced Optical Materials, 2(10):911–928, 2014.

[97] JP Goss, R Jones, SJ Breuer, PR Briddon, and Sven Öberg. The twelve-line 1.682 ev luminescence center in diamond and the vacancy-silicon complex. Physical review letters, 77(14):3041, 1996.

[98] A Sipahigil, RE Evans, DD Sukachev, MJ Burek, J Borregaard, MK Bhaskar, CT Nguyen, JL Pacheco, HA Atikian, C Meuwly, et al. An integrated diamond nanophotonics platform for quantum-optical networks. Science, 354(6314):847–850, 2016.

[99] Jennifer T. Choy, Birgit J. M. Hausmann, Thomas M. Babinec, Irfan Bulu, Mughees Khan, Patrick Maletinsky, Amir Yacoby, and Marko Lončar. Enhanced single-

photon emission from a diamond–silver aperture. Nature Photonics, 5(12):738–743, 2011.

[100] Young-Ik Sohn, Srujan Meesala, Benjamin Pingault, Haig A Atikian, Jeffrey Holz-grafe, Mustafa Gundogan, Camille Stavrakas, Megan J Stanley, Alp Sipahigil, Joon-hee Choi, et al. Engineering a diamond spin-qubit with a nano-electro-mechanical system. arXiv preprint arXiv:1706.03881, 2017.

[101] A. Sipahigil, K. D. Jahnke, L. J. Rogers, T. Teraji, J. Isoya, A. S. Zibrov, F. Jelezko, and M. D. Lukin. Indistinguishable photons from separated silicon-vacancy centers in diamond. Phys. Rev. Lett., 113:113602, Sep 2014.

[102] J. Riedrich-Moller, C. Arend, C. Pauly, F. Mucklich, M. Fischer, S. Gsell, M. Schreck, and C. Becher. Deterministic coupling of a single silicon-vacancy color center to a photonic crystal cavity in diamond. Nano Lett, 14(9):5281–7, 2014.

[103] Yousif A. Kelaita, Kevin A. Fischer, Thomas M. Babinec, Konstantinos G. Lagoudakis, Tomas Sarmiento, Armand Rundquist, Arka Majumdar, and Jelena Vučković. Hybrid metal-dielectric nanocavity for enhanced light-matter interactions. Opt. Mater. Express, 7(1):231–239, Jan 2017.

[104] K. T Shimizu, W. K Woo, B. R Fisher, H. J Eisler, and M. G Bawendi. Surface-enhanced emission from single semiconductor nanocrystals. Physical Review Letters,

89(11):117401, 2002.

[105] H. Sternschulte, K. Thonke, R. Sauer, P. C. Münzinger, and P. Michler. 1.681-ev luminescence center in chemical-vapor-deposited homoepitaxial diamond films. Phys. Rev. B, 50:14554–14560, Nov 1994.

[106] Srujan Meesala, Young-Ik Sohn, Haig A. Atikian, Samuel Kim, Michael J. Burek, Jennifer T. Choy, and Marko Lončar. Enhanced strain coupling of nitrogen-vacancy spins to nanoscale diamond cantilevers. Phys. Rev. Applied, 5:034010, Mar 2016.

[107] Kay D Jahnke, Alp Sipahigil, Jan M Binder, Marcus W Doherty, Mathias Metsch, Lachlan J Rogers, Neil B Manson, Mikhail D Lukin, and Fedor Jelezko. Electron–phonon processes of the silicon-vacancy centre in diamond. New Journal of Physics, 17(4):043011, 2015.